UNIVERSITY OF CALIFORNIA

Los Angeles

Variational Models for Illusory Contours and Shape Prior Segmentation

A dissertation submitted in partial satisfaction

of the requirements for the degree

Doctor of Philosophy in Mathmatics

by

Wei Zhu

2004

The dissertation of Wei Zhu is approved.

Stanley Osher

Luminita Vese

Dario Ringach

Tony F. Chan, Committee Chair

University of California, Los Angeles

2004

To my wife and my parents

TABLE OF CONTENTS

vi

List of Figures

xiii

Acknowledgments

I wish to express my sincere and deepest appreciation to my advisor, Prof. Tony F. Chan, for his guidance, advice and support throughout my graduate studies at UCLA. His enthusiasm, patience and intelligence have helped me achieve more in my studies. I would like to thank other members of my committee: Prof. Stanley Osher, Prof. Luminita Vese and Prof. Dario Ringach for their great help, encouragement and valuable suggestions during my study at UCLA. I would also like to thank Prof. Selim Esedoglu for his valuable discussions on various mathematical issues. Especially, I wish to express my sincere gratitude to Prof. Stanley Osher and Prof. Hailiang Liu for their great encouragement.

I would also like to thank other people for their generous help on mathematical topics as well as many aspects of my life. Thanks goes to Bing Song, Chiu-Yen Kao, Cho Hong Min, Mark Moelich, Fred Park, Ming-Ham (Andy) Yip, Jinjun Xu, Igor Yanovskiy, Sung Ha Kang, Haomin Zhou, Jianhong (Jackie) Shen, Richard Tsai, Berta Sandberg.

Vita

1973   Born, Anhui, P. R. China.

1994   B.S. (mathematics), Tsinghua University, P. R. China.

1999   M.S. (mathematics), Peking University, P. R. China.

1999–2004   Teaching Assistant and Research Assistant
                UCLA, Los Angeles, California

Presentations

Capturing illusory contours: a level set approach, Minisymposium at SIAM Conference on Image Science, Salt Lake City, UT, May 3-5, 2004.

Segmentation with depth: a level set approach, Minisymposium at SIAM Conference on Image Science, Salt Lake City, UT, May 3-5, 2004.

Abstract of the Dissertation

Variational Models for Illusory Contours and Shape Prior Segmentation

by

Wei Zhu

Doctor of Philosophy in Mathmatics

University of California, Los Angeles, 2004

Professor Tony F. Chan, Chair

This dissertation contains studies on variational models for illusory contours and shape prior segmentation problems.

Illusory contours are intrinsic phenomena in human vision. These contours are not completely made up of objects' boundaries, but part of them are missing. We propose two different level set based variational models to capture illusory contours. The first model is based on the relative locations between illusory contours and objects as well as the known shape information of the contours. The second approach utilizes curvature information via Euler's Elastica to complete missing boundaries. The method is capable of a wide-range of illusory contours. As an extension of illusory contours, we use level set methods to numerically solve the minimization problem of the Nitzberg-Mumford-Shiota's functional that appears in segmentation with depth problem, since one of the key problems for this topic is to reconstruct missing boundaries of farther objects that are occluded by nearer objects.

Shape prior segmentation is to incorporate shape information into the standard intensity based segmentation procedure. This is always necessary because standard segmentation methods fail to segment meaningful objects when they are in low gray contrasts or occluded by other ones. We propose a level set based variational model that combines Chan-Vese's segmentation model and the shape comparison term using the Heaviside function.

CHAPTER 1

Introduction

Image processing is becoming a more and more active branch of applied mathematics with its broad applications. Typical image processing tasks include segmentation, denoising, debluring, and compression. In this dissertation, we focus our attention on image segmentation, which includes the problems on capturing illusory contours and shape prior segmentation.

Many kinds of mathematical theories have been applied to the problems in image processing. These methods mainly involve partial differential equations, variational methods, statistical methods, and even differential geometry, Lie groups. In this dissertation, we are interested in using variational methods to characterize image processing problems. Variational methods are very popular methods. It is flexible for us to construct models for particular applications. And the intrinsic partial differential equations, i.e., Euler-Lagrange equations from variational models, come out more naturally than artificial ones. Moreover, in the mathematical point of view, it is relatively easier to provide analytical results for the partial differential equations originated from variational models than for general partial differential equations.

1.1 Illusory contours

Illusory contours are intrinsic phenomena in human vision. These contours are not completely made up of existing objects' boundaries, but part or even all of them are totally missing. Classical examples include the Kanizsa triangle and square [Kan79] shown in Figure 1.1. When human being looks at these figures,

(a) $\qquad\qquad$ (b)
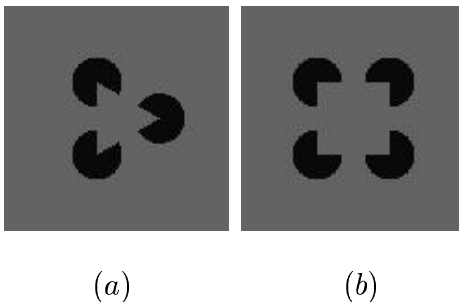
Figure 1.1: (a) Kanizsa triangle, (b) Kanizsa square.

it is easy for him to recognize a triangle and a square even though parts of their boundaries are not present. However, it is a challenging problem in computer vision. Because it can not be regarded as a standard segmentation problem from which one can only "find" existing boundaries of objects.

In fact, there are many kinds of illusory contours in human perception. In this dissertation, besides the above kind of illusory contours (Figure 1.1), we also consider missing boundaries (illusory contours) in the problem of segmentation with depth. Segmentation with depth is different form standard segmentation. Its goal is to automatically infer the shapes of objects and the occlusion relations among them. Figure 1.2 is an example to illustrate the difference between standard segmentation and segmentation with depth.

Front   Behind
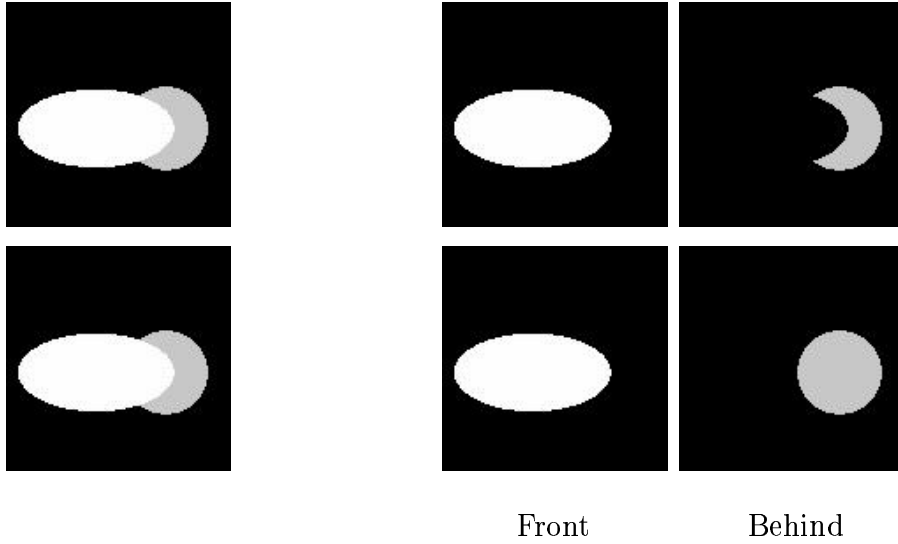
Figure 1.2: The first row contains the original image (Left) with two regions (middle and right) given by any multi-phase intensity based segmentation method, and the second row illustrates the results from a segmentation with depth model. Besides the occlusion relation between the two objects ("Front" and "Behind" in this example), the missing boundary of the behind object is also restored.

1.2   Shape prior segmentation

Segmentation is a fundamental problem among all topics in the field of image processing. Segmentation is briefly to decompose a given image domain into several pieces regions in each of which the gray intensity distribution is homogeneous.

However, standard segmentation methods (intensity based methods) always fail to segment meaningful objects from given images when the objects are in low contrast or are occluded by others. To this end, one has to resort to the shape information of the meaningful objects. This incorporation of shape information into segmentation process is always called shape prior segmentation. In Figure

3

1.3, we present an example that illustrates a hand is segmented from a given image with its shape information.

Figure 1.3: In this example, we show that an occluded hand can be segmented from an image by using the shape information of a similar hand.

1.3 Contributions and Organization of This Dissertation

In this dissertation, we are focusing our attention on the problems of illusory contours and shape prior segmentation.

Many mathematical methods, for instance in [GKP96, GPR98, PGR99, SMS00], have been proposed to capture illusory contours. In Chapter 2 and Chapter 3, we present two different variational models to deal with this problem. In Chapter 2, we employ shape information to identify illusory contours. We assume that the shape of the desirable illusory contour is known, but its location, rotation and scale are unknown. Then we search inside the given image for a contour (with the known shape) that matches the desirable illusory contour by using the location relations between objects and the desirable illusory contours. Moreover, we extend the case of orthogonal transformations of shape to more general cases of affine transformations, which allows us to identify more illusory contours with

4

a given shape.

In Chapter 3, we construct a variational model that utilizes curvature information to capture illusory contours. Basically, the key thing for illusory contours is to complete missing contours. We employ Euler's elastica [Mum94, CKS02] to control an active contour so that it can complete missing contours in a smooth way. Our model also preserves real junctions very well by emphasizing the information near these junctions in our model, which also conforms to human vision. The model is capable of a wide range of illusory contours regardless of curves or straight lines as missing boundaries.

As an extension of illusory contours (see Figure 1.2), in Chapter 4, we use level set methods [OS88] to numerically solve the minimization problem of the Nitzberg-Mumford-Shiota's functional [NMS93] that appears in segmentation with depth problem. By using level set methods, curvature terms can be represented directly, which is much more easier and accurate than using the approximation via $\Gamma-$ convergence in [EM03]. The above minimization problem then turns out to be solving a system of fourth order equations, which is similar to the Euler Lagrange equations derived in Chapter 3. We use Smereka's semi-implicit method [Sme03] to solve the fourth order equations, which speeds up the evolution process considerably.

In Chapter 5, we address the problem of shape prior segmentation. In the literature, there are lots of works on this topic. For instance, in [LFG00, LGF00, CTT02], the authors incorporated shape information (statistical or level set method based) into Caselles et al.'s geometric active contours model [CKS97]; in [CTW02], a region-based variational model that introduces statistical shape

knowledge into Mumford-Shah functional [MS89, MS95] was proposed. Later, Cremers et. al. introduced a labelling function into shape prior segmentation process in [CSS03]. This labelling function helps to determine the regions with which the given shape should be compared. Inspired by this idea, we present in this chapter a level set based variational model to the shape prior segmentation problem. Our model is different from [CSS03] mainly in two aspects. On one hand, our approach permits scaling, translation and rotation of the given shape. On the other hand, we take a different shape comparison term which is independent of the image domain. Moreover, we provide a proof for a fast principle, which is also mentioned [GF02] and similar to [SC02], for minimizing Chan-Vese's segmentation model without length term. We extend the principle to the minimization of our prescribed functional.

CHAPTER 2

Capturing illusory contours using shape information

2.1 Introduction

Illusory contours are common phenomena in human vision. These contours are not completely made up of existing objects' boundaries, but part of them are not present. Classical examples include the Kanizsa triangle and square [Kan79, PM87] shown in Figure 2.1. Human visual system has no trouble filling in the missing boundaries for the illusory triangle and square. However, capturing illusory contours can not be simply regarded as a standard segmentation problem since segmentation methods only "find" existing boundaries of objects. Therefore, the major computational challenge of identifying illusory contours is to complete the absent contours.

It is not fully understood how humans perceive illusory contours. Psychologists have known for some time that certain visual cues such as corners, T-junctions or L-junctions and boundaries are important in this process. Many computational models have been proposed to capture illusory contours. They can be categorized into two kinds. One kind involves completing the boundary of special interests by using the information of corners and boundaries, such as

7

in Geiger et. al. [GPR98, GKP96], Ulman [Ulm76], etc. The other kind employs information about the whole region instead of corners and boundaries; see e.g. Sarti, Mallidi and Sethian [SMS00].

Figure 2.1: Kanizsa triangle, square and a special illusory triangle. Human being may easily identify a triangle and a square in the first two pictures respectively. However, in the right most picture, without the shape information of triangle, the illusory triangle may not be recognized.

In [GPR98], Geiger et al. decompose images into several layers with the illusory contours in a different layer from those of real objects or background. They first pick out all the corners in the image, including T-junctions and L-junctions, then set out a set of hypothesis for each corner according to whether they belong to different layers. The best set of hypothesis is determined by minimizing an appropriate form of energy functional, from which the illusory contour can be obtained. Taking a different perspective, Sarti et al. [SMS00, SC01] begin with an initial surface, which is chosen on the basis of a reference fixation point inside the region bounded by desirable illusory contours, then flow the surface according to the image gradient. The flow is chosen to sharpen the surface around the existing edges and complete the missing edges.

In this chapter, we posit that shape information has a role to play in cap-

turing illusory contours. For example, in the right most picture of Figure 2.1, it would be difficult to perceive the triangle without a priori knowledge of its shape. We therefore would like to propose a mathematical model to incorporate shape information in identifying illusory contours. Our idea is this: we first assume the shape of the illusory contour is known, then we search in the equivalence class (discussed in section 2.2.1) of the known shape for a suitable contour that matches the illusory contour perfectly. For instance, we characterize the Kanizsa triangle as the best equilateral triangle that fits the given image (the precise definition of fit will be discussed later). Here, we consider only one shape. But in general, we expect the methodology can be extended to a library of shapes.

Our method differs from others in several ways. First, our method incorporates shape information to capture illusory contours. Second, because the known shape can be arbitrary, with rather complicated geometry, our method can identify illusory contours with curved as well as straight boundaries. Third, in our method, there is no extra computational cost associated with finding and analyzing visual cues such as T-junctions and L-junctions. Finally, in our method, the initial guess for the illusory contour can be put anywhere in the image without requiring the specification of a reference fixation point.

The remain part of this chapter is organized as follows. Section 2.2 consists of several parts. In subsection 2.2.1, a review for shape representation using signed distance functions is given. Then two models are discussed in subsection 2.2.2 and 2.2.3 respectively. In section 2.3, we present two groups of experiments, including the Kanizsa triangle, square and some synthetic examples. A conclusion is given in section 2.4, which is followed by an appendix in section 2.5 for the formulation

of the gradient descent used in this chapter.

2.2 Models

2.2.1 Shape representation using signed distance functions

As discussed in Paragios et. al.'s work [PRR02, RP02], we can use signed distance functions (special level set functions [OS88]) to represent shapes. Given an object $\Omega \subset R^2$, which is assumed to be closed and bounded, then there is a unique viscosity solution to the following equation:

$$| \nabla \phi | = 1$$

$$\phi \begin{cases} > 0 \ x \in \Omega \backslash \partial \Omega \\ = 0 \ x \in \partial \Omega \\ < 0 \ x \in R^2 \backslash \Omega. \end{cases} \tag{2.1}$$

In this way, any object (or region) in the plane corresponds to a unique signed distance function, and vice versa. As shape is invariant to translation, rotation and scaling, we may define an equivalence relation in the collection of objects in the plane. Any two objects are said to be *equivalent* if they have the same shape. Their signed distance functions are related. For example, let Ω_1 and Ω_2 be two objects with the same shape, ϕ_1 and ϕ_2 be the signed distance functions respectively, then there exists a four-tuple (a, b, r, θ) such that:

$$\phi_2(x, y) \ = \ r\phi_1[\frac{(x - a)\cos\theta + (y - b)\sin\theta}{r}, \frac{-(x - a)\sin\theta + (y - b)\cos\theta}{r}],$$

$$\tag{2.2}$$

where (a, b) represents the center, r the scaling factor and θ the angle of rotation.

Equivalently, we can write as $\phi_2 = r\phi_1 \circ \left(\frac{1}{r}T\right)$, where

$$T\left(\begin{pmatrix} x \\ y \end{pmatrix}\right) = \begin{pmatrix} \cos\theta & \sin\theta \\ -\sin\theta & \cos\theta \end{pmatrix}\begin{pmatrix} x - a \\ y - b \end{pmatrix}. \tag{2.3}$$

Note that the matrix $\begin{pmatrix} \cos\theta & \sin\theta \\ -\sin\theta & \cos\theta \end{pmatrix}$ in (2.3) is an orthogonal matrix. In general, we may also choose a general matrix in (2.3), not merely an orthogonal one. This would allow our method to find illusory contours that are close but not necessarily an exact match of a known shape. We consider both cases in this chapter.

2.2.2 The model for exact shapes

In this chapter, we only consider binary images, which take the value of 1 on the regions occupied by "objects" and 0 on the "background" in the defined domain. In fact, general images can be pre-processed to be this kind of images. Any region based segmentation models, such as Chan and Vese's model [CV01], could separate objects from background and yield a level set function with positive values in the regions occupied by objects and negative values in the background. We can then get a desirable image from the level set function by using the Heaviside function.

Therefore, we can assume the given image u to be a binary image defined in domain $R \subset R^2$, with $u = 1$ on the objects, $u = 0$ on the background. For example, in the Kanizsa triangle in Figure 2.1, $u = 1$ on the black parts and 0 on the remaining part. In addition, we assume that the illusory contour takes a known shape represented by a signed distance function ϕ_0 in its equivalence

class. Let ϕ be the signed distance function of the candidate illusory contour that belongs to the equivalence class.

We will now define an energy functional finding the ϕ in the equivalence class of ϕ_0 which best matches the information for the illusory contour given in the image u. The challenge is to measure this match without knowing the complete boundary of the illusory figure. Our particular approach is as follows. We shall first characterize the illusory contour in u as having the following two properties:

- 1. Since parts of the boundary of the desirable illusory figure is made up by parts of the objects (in particular the boundaries) in u, we want the candidate illusory contour to be close to the objects in u.

- 2. As we want the objects in u to border but not overlap with the candidate illusory figure, the overlap between them should be minimized.

We will take advantage of shape representation using signed distance functions to construct an energy satisfying the two requirements. Employing the distance is the key ingredient of our model.

For the first requirement, we recall that since ϕ is the signed distance function of the candidate illusory figure, $\left|\phi(p)\right|$ measures the distance from any point $p \in R$ to the candidate illusory contour, i.e., $\phi = 0$. As we want the candidate illusory contour to be close to all the objects, the sum of the distances from each point of the objects to the candidate illusory contour should be small. We choose the following integral to represent this sum:

$$\int_R u\phi^2 dxdy. \tag{2.4}$$

Here, we include u because we only want to count the distances from the points of the objects (defined by $u = 1$) not the background $u = 0$ to the candidate illusory contour. An illustration in Figure 2.2 shows that different candidate illusory contours yield different values of the integral.

Figure 2.2: The term $\int_R u\phi^2 dxdy$ for the right figure is smaller than that of the left because the candidate illusory contour (white curve) in the right figure is more close to the objects than the left one.

Similarly, for the second requirement, we propose a term:

$$\int_R uH(\phi)\phi^2 dxdy, \tag{2.5}$$

where $H(\cdot)$ is the Heaviside function:

$$H(x) = \begin{cases} 1 & x > 0 \\ 0 & x \leq 0. \end{cases}$$

Note that the term $uH(\phi) = 1$ only in the overlapping region between the region bounded by the candidate illusory contour and the objects in the image. Therefore the term (2.5) is the sum of the distances from all overlapping points to the candidate illusory contour, i.e., $\phi = 0$.

We combine the two terms in the following energy functional:

$$\int_R u\phi^2 dxdy + \lambda \int_R uH(\phi)\phi^2 dxdy, \tag{2.6}$$

Figure 2.3: In this figure, the candidate illusory contour (white curve) is trapped into a local minimizer of (2.6), since a smaller change of (a, b, r, θ) will not make (2.6) smaller.

where λ is a parameter that balances the two terms.

However, this model is insufficient because the candidate illusory contour can easily be trapped in a local minimizer. For example in the situation shown in Figure 2.3, the candidate illusory contour is in a local minimizer because perturbing its left vertical boundary (or changing the scale) will decrease neither the first term (in this situation, for each point inside the objects, the closest point on $\phi = 0$ is on the other two boundaries of the candidate illusory figure) nor the second term (since moving this boundary will not change the overlap).

This case only occurs when the candidate illusory contour is bigger than the desirable one. Therefore, a simple way to overcome this problem is to introduce a term in the energy functional to exert a preference for a candidate illusory contour with a small scale. Hence, we can modify the second term in (2.6) as follows:

$$\lambda \int_R uH(\phi)(\phi + rL)^2 dxdy, \tag{2.7}$$

where L is a scale constant compensating for the dimension difference between ϕ and r. This means if there is overlapping, a smaller scale r is required.

Consequently, we have the combined energy functional:

$$E(a, b, r, \theta) = \int_R u\phi^2 dxdy + \lambda \int_R uH(\phi)(\phi + rL)^2 dxdy, \qquad (2.8)$$

where λ controls how much the overlap is allowed, L is the same as mentioned above, and

$$\phi(x, y) = r\phi_0[\frac{(x-a)\sin\theta + (y-b)\cos\theta}{r}, \frac{-(x-a)\sin\theta + (y-b)\cos\theta}{r}],$$

and $H(\cdot)$ is the Heaviside function.

Remark 1: The energy (2.8) involves the four-tuple (a, b, r, θ) which represents different contour in the same shape equivalence class. To minimize the energy is to update the four-tuple, instead of ϕ itself. Therefore, it is fast to minimize the energy. In fact, we only need to calculate some integrals on the image domain (see the appendix).

Remark 2: Our model is constructed to find "interior" illusory contours. If we replace $H(\phi)$ by $1 - H(\phi)$ in (2.6) so that the energy functional takes the form:

$$E(a, b, r, \theta) = \int_R u\phi^2 dxdy + \lambda \int_R u(1 - H(\phi))\phi^2 dxdy, \qquad (2.9)$$

we can also find "exterior" illusory contours.

Remark 3: The distribution of objects inside a given image is important to our model. Our model will fail to deal with those cases that objects distribute far from symmetrically in area around the desirable illusory contour. This is because of the first term in our model.

2.2.3 The model for affine shapes

As discussed in section 2.2.1, if we choose a general matrix instead of an orthogonal one, we may capture illusory contours whose shapes are affine transformation of the given shape. This allows a larger class of illusory contours to be found for only one known shape. However, some restriction should be added to the matrix; otherwise, the shape of the candidate illusory figure could be too different from the known shape. For instance, in Figure 2.4, a disk could become a sharp ellipse. Hence, a new term of controlling the matrix $A = \begin{pmatrix} a_{11} & a_{12} \\ a_{21} & a_{22} \end{pmatrix}$ should be included in our model.
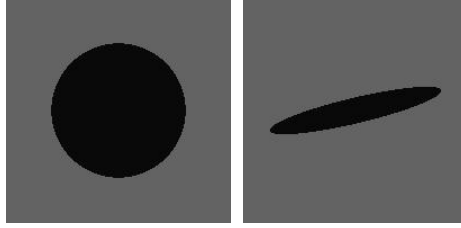
Figure 2.4: The left figure is a disk, while the right one is an ellipse which is a transformation from the left by matrix $A = [5, 1; 1, 1]$.

Here, we consider the term $\parallel AA^T - I \parallel_2^2$. $\parallel \cdot \parallel_2$ is the ordinary 2-norm of matrix. We set up a threshold ϵ. When $\parallel AA^T - I \parallel_2^2 > \epsilon$, the amount should decrease.

Therefore, the new energy reads:

$$
\begin{aligned}
E(a, b, r, a_{11}, a_{12}, a_{21}, a_{22}) &= \int_R u\phi^2 dxdy + \lambda \int_R uH(\phi)(\phi + rL)^2 dxdy \\
&\quad + \mu H(\parallel AA^T - I \parallel_2^2 - \epsilon),
\end{aligned} \tag{2.10}
$$

16

where λ and L are two parameters, with λ controlling the overlapping between the region bounded by the candidate illusory contour and the objects, L is a scaling constant compensating for the scale difference between ϕ and r; ϵ is the threshold controlling how much the affine transformation compared with an orthogonal one can be allowed, μ is a parameter as well. And ϕ becomes:

$$\phi(x,y) = r\phi_0\left[\frac{a_{11}(x-a)+a_{12}(y-b)}{r}, \frac{a_{21}(x-a)+a_{22}(y-b)}{r}\right]. \quad (2.11)$$

Remark 4: In (2.11), ϕ is not a signed distance function any more unless A is an orthogonal one. But it is close. In fact, $\mid \nabla\phi \mid^2 = \begin{bmatrix} \phi_x & \phi_y \end{bmatrix} \begin{bmatrix} \phi_x & \phi_y \end{bmatrix}^T = \begin{bmatrix} \phi_{0x} & \phi_{0y} \end{bmatrix} AA^T \begin{bmatrix} \phi_{0x} & \phi_{0y} \end{bmatrix}^T \approx \mid \nabla\phi_0 \mid^2$, since $\parallel AA^T - I \parallel_2^2$ is very small. It also shows that the requirement of A is necessary if we take advantage of signed distance functions in our model.

2.3   Experiments

We employ the conventional gradient descent method to minimize the above energy (2.8) and (2.10). To this end, the four-tuple (a, b, r, θ) are assumed to be the functions about time t, then the energy is a function of t as well. The detail will be discussed in the appendix.

In this section, we first present two groups of results, one for the exact shapes, including the Kanizsa triangle and square, and the other for the affine shapes, including general triangle, parallelogram and ellipse, which are affine transformations of equilateral triangle, square and disk respectively. Second, a comparison of searching for different illusory contours by the second model with the same specified shape will be given.

17

In the following, each of the results consists of a process of searching for illusory contours, starting from the initial guess, and ending at the candidate illusory contour in the convergent state. The order is from top row to bottom row, from left to right. Additionally, we use white curves to represent the candidate contours.

All the images are 120×120, defined on the domain $[-4, 4] \times [-4, 4]$, and $L = 1$. Different parameters and time step dt are chosen accordingly to each experiment.

2.3.1 Experiments for exact shapes

The first two examples are the Kanizsa triangle and square (Figure 2.5 and 2.6). We search for them with the shape of equilateral triangle and square respectively. It can be seen that as time evolves, the candidate contours will match the desirable illusory contours perfectly.

The third example (Figure 2.7) is still an illusory equilateral triangle. In this example, the corner of the triangle are not shown as any visual cues such as L-junction or T-junctions. Any method that uses this information will not be applicable for this case. Without the shape of triangle, the illusory contour here is difficult to be recognized. However, as our model incorporates shape information, it still can identify the illusory triangle.

The illusory contours are disks or circles in the next two examples (Figure 2.8 and 2.9). One is a classical illusory contour, with a disk in a square, the other is a disk in an triangle. These two examples show that illusory contours with curved boundaries can also be handled with our model.

The next example (Figure 2.10) is an illusory triangle immersed in a group of black bars. It is different from not only the Kaniza triangle but also the third example. First, none of the corners of the illusory triangle has to be a L-junction or T-junction. Second, it touches the bars not by its continuous boundaries but by several discrete parts. This example illustrates that our model is also capable of singling out illusory contours from some "messy" environment. Figure 2.11 is also this kind of image with an illusory square immersed in four groups of annuli.

The last example for this case is a Rubin Vase (Figure 2.12). In this image, one may recognize two faces or only a Rubin Vase. This example shows that our model is also capable of identifying complicated illusory contours.
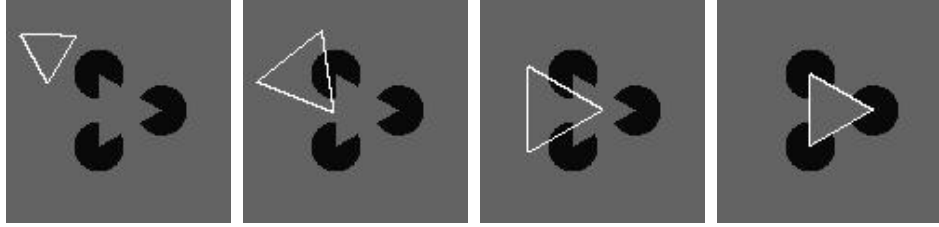
Figure 2.5: Searching for Kanizsa triangle in the equivalence class of an equilateral triangle. In this experiment, time step size $dt = 0.01$, $\lambda = 2.0$.

Figure 2.6: Searching for Kanizsa square in the equivalence class of a square. In this experiment, time step size $dt = 0.01$, $\lambda = 2.0$.

2.3.2 Experiments for affine shapes

In this section, we show some experiments for the affine case and a comparison of searching for different illusory contours with the same specified shape and initial candidate contour. In these examples, the known shapes are equilateral triangle, square and circle.

The first example (Figure 2.13) is to search for a general illusory triangle (not an equilateral triangle), starting from an initial equilateral triangle, in the class of contours whose shapes are transformations of an equilateral triangle. From the group of figures, we can see that as time evolves, the candidate illusory contour will converge to the desirable ones. Moreover, during the process, the shape of each candidate illusory contour is unnecessarily exact as the known shape, but keeps close to the later one.

The second and third examples (Figure 2.14 and 2.15) are an illusory parallelogram and ellipse respectively. Similarly as the first example, the candidate illusory contours converge to the desirable illusory ones.

The next two examples (Figure 2.16 and 2.17) are comparisons of searching

Figure 2.7: Searching for an illusory triangle in the equivalence class of an equilateral triangle. In this experiment, time step size $dt = 0.02$, $\lambda = 1.5$.

Figure 2.8: Searching for an illusory disk in the equivalence class of a disk. In this experiment, time step size $dt = 0.05$, $\lambda = 0.2$.
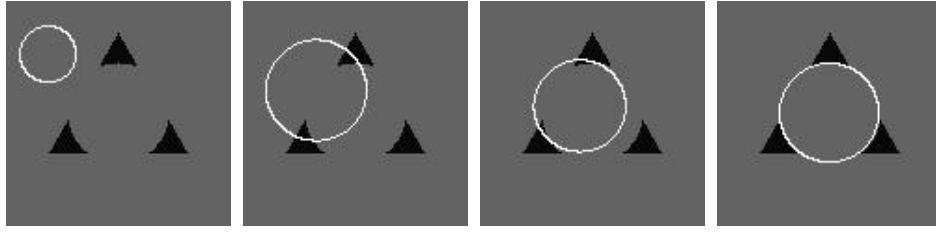
Figure 2.9: Searching for an illusory disk in the equivalence class of a disk. In this experiment, time step size $dt = 0.05$, $\lambda = 0.5$.

for different illusory contours with the same known shape and initial candidate illusory contour. These two examples show that the model for affine shapes allows a larger shape class of illusory contours than the model for exact shapes. In fact, the first model is just a special case of the second one.

2.4 Conclusion

In this chapter, we employ shape information to capture illusory contours. We propose a variational model by taking advantage of the location relations between illusory contours and objects. We consider two cases: one is to search for illusory
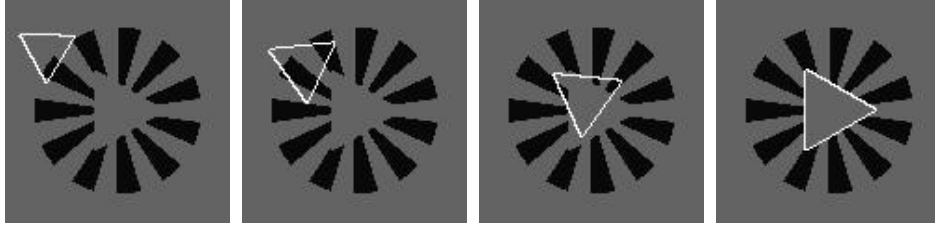
Figure 2.10: Searching for an illusory triangle in the equivalence class of an equilateral triangle. In this experiment, time step size $dt = 0.002$, $\lambda = 6.0$.
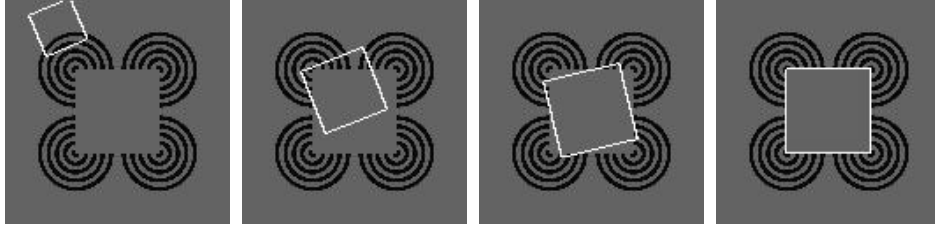
Figure 2.11: Searching for an illusory square in the equivalence class of a square. In this experiment, time step size $dt = 0.001$, $\lambda = 4.0$.

contours whose shapes are as exact as known shapes while the second case is for illusory contours whose shapes are affine transformations of given shapes, which makes our method be applicable for a broad class of illusory contours. The experiments listed validate our models.

2.5   Appendix

In this appendix, we derive the formulas for decreasing the energy $E(a, b, r, \theta)$ with the conventional gradient decent method.

22

Figure 2.12: Searching for an illusory Rubin Vase in the equivalence class of a Rubin Vase. In this experiment, time step size $dt = 0.001$, $\lambda = 4.0$.
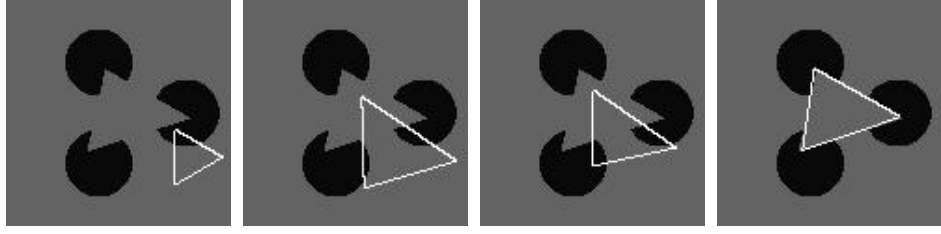
Figure 2.13: Searching for an illusory triangle (not an equilateral triangle) in the class of shapes which are transformations of an equilateral triangle. In this experiment, time step size $dt = 0.01$, $\lambda = 2.0$, $\mu = 100.0$ and $\epsilon = 0.2$.

We assume that (a, b, r, θ) are functions of time t. Consequently,

$$
\begin{aligned}
\frac{dE}{dt} &= \int_R [2u\phi \frac{d\phi}{dt} + \lambda u \delta(\phi)(\phi + rL)^2 \frac{d\phi}{dt} \\
&\quad + 2\lambda u H(\phi)(\phi + rL)(\frac{d\phi}{dt} + L\frac{dr}{dt}))]dxdy \\
&= \int_R u[2\phi + \lambda \delta(\phi)(\phi + rL)^2 + 2\lambda H(\phi)(\phi + rL)]\frac{d\phi}{dt}dxdy \\
&\quad + \int_R [2\lambda u H(\phi)(\phi + rL)L]\frac{dr}{dt}dxdy, \quad\quad (2.12)
\end{aligned}
$$

where $\delta(\cdot)$ is derivative of Heaviside function $H(\cdot)$ in the distribution sense.

For simplicity, we denote

$$
A = u[2\phi + \lambda \delta(\phi)(\phi + rL)^2 + 2\lambda H(\phi)(\phi + rL)],
$$
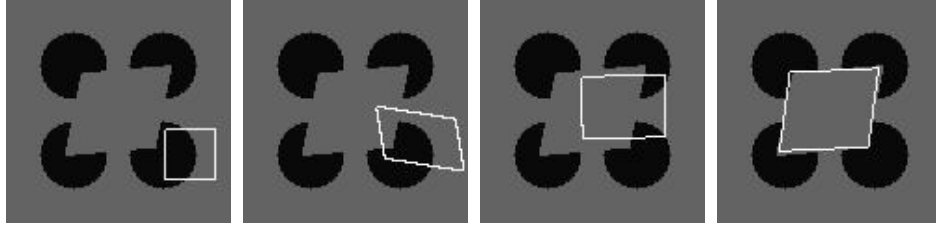
Figure 2.14: Searching for an illusory parallelogram (not a square)in the class of shapes which are transformations of a square. In this experiment, time step size $dt = 0.0075$, $\lambda = 2.0$, $\mu = 100.0$ and $\epsilon = 0.2$.
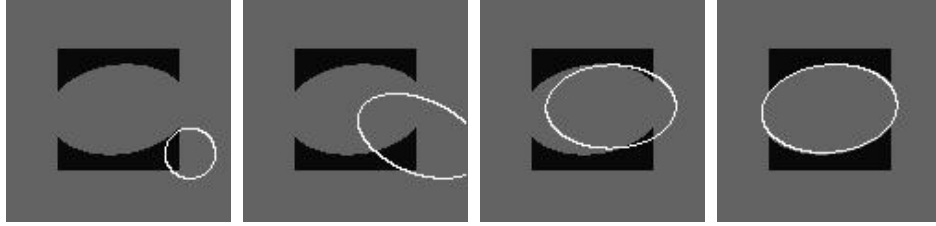
Figure 2.15: Searching for an illusory ellipse (not a disk)in the class of shapes which are transformations of a disk. In this experiment, time step size $dt = 0.01$, $\lambda = 0.5$, $\mu = 100.0$ and $\epsilon = 0.4$.

then

$$\frac{dE}{dt} = \int_R A\frac{d\phi}{dt}dxdy + \int_R 2\lambda u H(\phi)(\phi + rL)L\frac{dr}{dt}dxdy.$$

Since

$$\begin{aligned}
\frac{d\phi}{dt} &= [-\phi_0 + \phi_{0x}\frac{(x-a)\cos\theta + (y-b)\sin\theta}{r}\\
&+\phi_{0y}\frac{-(x-a)\cos\theta + (y-b)\sin\theta}{r}](\frac{-dr}{dt})\\
&+(\phi_{0x}\cos\theta - \phi_{0y}\sin\theta)(-\frac{da}{dt}) + (\phi_{0x}\sin\theta + \phi_{0y}\cos\theta)(-\frac{db}{dt})
\end{aligned}$$

$$+[\phi_{0x}((x-a)\sin\theta - (y-b)\sin\theta) + \phi_{0y}((x-a)\cos\theta + (y-b)\sin\theta)](-\frac{d\theta}{dt}),$$

24
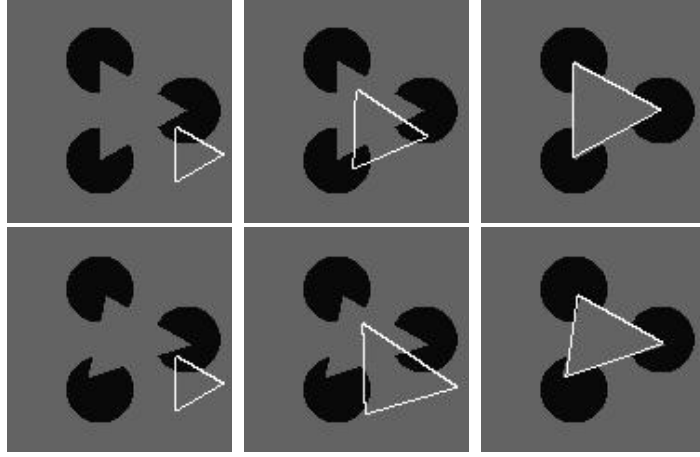
Figure 2.16: The top row is the searching process (initial, intermediate and final step, from left to right) for Kanizsa triangle. With the same initial candidate illusory contour, another searching process for a general triangle is shown in the bottom row. They are both done by the model for affine shapes. The comparison validates that this model can be applied for finding some general triangles with the shape of an equilateral triangle.

where $\phi_{0x} = \partial\phi_0/\partial x$ and $\phi_{0y} = \partial\phi_0/\partial y$, if we choose

$$\frac{da}{dt} = \int_R A(\phi_{0x}\cos\theta - \phi_{0y}\sin\theta)dxdy, \tag{2.13}$$

$$\frac{db}{dt} = \int_R A(\phi_{0x}\sin\theta + \phi_{0y}\cos\theta)dxdy, \tag{2.14}$$

$$\frac{dr}{dt} = \int_R A[-\phi_0 + \phi_{0x}\frac{(x-a)\cos\theta + (y-b)\sin\theta}{r}$$
$$+\phi_{0y}\frac{-(x-a)\sin\theta + (y-b)\cos\theta}{r}]dxdy$$
$$-\int_R 2\lambda u H(\phi)(\phi + rL)Ldxdy, \tag{2.15}$$

$$\frac{d\theta}{dt} = \int_R A\{\phi_{0x}[(x-a)\sin\theta - (y-b)\cos\theta]$$
$$+\phi_{0y}[(x-a)\cos\theta + (y-b)\sin\theta]\}dxdy, \tag{2.16}$$
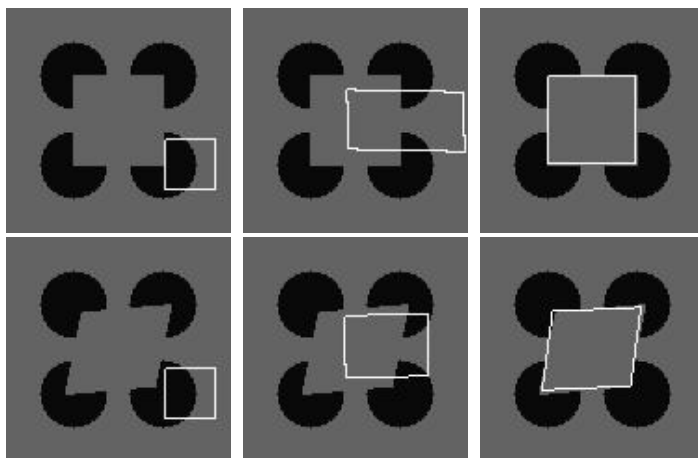
Figure 2.17: The top row is the searching process (initial, intermediate and final step, from left to right) for Kanizsa square. With the same initial candidate illusory contour, another searching process for a general parallelogram is shown in the bottom row.

then $\frac{dE}{dt} \leq 0$, which means the energy will decrease.

Similarly, we can derive the formulas for the model for affine shapes.

CHAPTER 3

Capturing illusory contours using curvature information

3.1 Introduction

As discussed in the last chapter, illusory contours are intrinsic phenomena in human perception. The salient character and major computational challenge of illusory contours is that part of their boundaries are missing. Both of the related work mentioned in the last chapter yield excellent illusory contours when missing boundaries are straight lines, but they are incapable of curved missing boundaries. Moreover, our model in the last chapter highly depend on known shapes of illusory contours, which are not available for general cases.

In this chapter, we propose a level set based variational model to this problem. Basically, the key thing for recognizing illusory contours is to complete the absent boundaries. Our idea is to integrate the incomplete contours in a smooth way by incorporating Euler's elastica, which conforms to human vision. Specifically, we embed the candidate illusory contour as the zero level set of a function, and then update the level set function in a way such that its zero level set will steer to the inside desired boundaries and stick to them (especially those real junctions) while complete missing boundaries smoothly.

The remain part of this chapter is organized as follows. In section 3.2, Sarti et. al.'s PDE based method [SMS00] is reviewed, and we point out why the method is not applicable to those cases with curved missing boundaries. In section 3.3, we propose a level set based variational model as well as discuss the numerical algorithms. Numerical results are presented in section 3.4, including many classical illusory contours. Finally, a conclusion is made in section 3.5.

3.2 Sarti et al's method for completing missing boundaries

There are many works in the literature on identifying illusory contours. In this section, we only review Sarti et al's model [SMS00] in detail, since their model is a variational one instead of a combinatorial or statistical based model, and is closely related to our work.

Let $I : \Omega \to \mathbf{R}$ be an image defined on a rectangle Ω. Firstly, Sarti et. al. build a representation called the "law primal sketch" to detect the intensity changes and vision cues such as orientation of structures and T-junctions. Specifically, they consider an edge indicator as follows:

$$
\begin{aligned}
g(x, y) &= \frac{1}{1 + (|\nabla G_\sigma(x, y) \star I(x, y)|/\beta)^2} \\
G_\sigma(\xi) &= \frac{exp(-(|\xi|/\sigma)^2)}{\sigma\sqrt{\pi}},
\end{aligned}
\tag{3.1}
$$

where β and σ are scale parameters which determine the minimal size of the details to be detected. Thus, the value g is close to 0 in the regions where the image intensity changes significantly, i.e., the boundaries, and is close to 1 in homogeneous regions.

Secondly, they consider a surface $S : (x, y) \rightarrow (x, y, \Phi(x, y))$ which is also defined on the domain Ω, and then construct a weighted surface area of S by incorporating the edge indicator function g. It reads:

$$\int_\Omega g(x, y) \sqrt{1 + \Phi_x^2 + \Phi_y^2} dx dy, \tag{3.2}$$

and then the evolution equation for Φ is:

$$\frac{\partial \Phi}{\partial t} = g \frac{(1 + \Phi_x^2)\Phi_{yy} - 2\Phi_x \Phi_y \Phi_{xy} + (1 + \Phi_y^2)\Phi_{xx}}{1 + \Phi_x^2 + \Phi_y^2} + (g_x \Phi_x + g_y \Phi_y). \tag{3.3}$$

As Φ is updated according to (3.3), the surface will become flat in homogeneous regions in which g takes the value 1. However, on the existing edges, the sharp of the surface can be allowed because g takes the value 0. In this way, if the initial surface is chosen appropriately, the steady state surface will consist of several levels of flat surfaces, one of which can be used to identify illusory contours.

In fact, the choice of the initial surface is crucial to this method. To this end, Sarti et. al. choose a fixation point (gaze point) inside the region bounded by the goal illusory contour, then set up an initial surface on the basis of the point. For example, they select the initial Φ to be α/D, where D is the distance function to the fixation point and α is a scaling factor. With this initial surface, the flow (3.3) will flatten the surface as well as sharpen it on the existing boundaries and thus connect the missing boundaries. Then the illusory contour can be identified as the boundary of the highest layer of the surface.

The method can be applied to identify illusory contours efficiently. However, as for completing missing boundaries, the model privileges straight lines, which may be inapplicable to many illusory contours. As discussed in [SMS00], it can be

seen that around the sharp surface, or the illusory contours, the spatial derivatives will be very large, i.e., $|\Phi_x|, |\Phi_y| \gg 1$. Thus, the flow (3.3) approximates to

$$\frac{\partial \Phi}{\partial t} \approx g \frac{\Phi_x^2 \Phi_{yy} - 2\Phi_x \Phi_y \Phi_{xy} + \Phi_y^2 \Phi_{xx}}{\Phi_x^2 + \Phi_y^2} + (g_x \Phi_x + g_y \Phi_y). \qquad (3.4)$$

Then the first term is nothing but $g\kappa(\Phi)|\nabla\Phi|$, where $\kappa(\Phi) = \nabla \cdot (\nabla\Phi/|\nabla\Phi|)$ represents curvatures of level curves. Moreover, due to $g = 1$ on the missing boundaries, the first term becomes $\kappa(\Phi)|\nabla\Phi|$, which is the variation of length terms of level curves and thus will straighten the curves during the evolution of Φ. This fact verifies that the model prefers using straight lines to complete missing boundaries.

3.3 Our model and the numerical algorithm

In this section, we present a level set based variational model to identify illusory contours as well as the numerical algorithms.

Basically, we evolve a level set function such that its zero level set locates the goal illusory contour. To this end, two problems need to be considered. One is how to drive the zero level set to the desired boundaries, and the other is how to complete missing boundaries. For the first problem, we will take advantage of the distance function defined according to the boundaries of the objects inside the image. We thus define a curve integral which measures the sum of distances from the zero level set to objects' boundaries. Minimizing this integral will steer the zero level set to the boundaries. For the second problem, to remedy the inability of Sarti et al's method to complete missing boundaries using general curves for complicated shape, we will employ Euler's elastica [Mum94, CKS02]. Euler's

elastica permits general smooth curves instead of only straight lines to complete missing boundaries.

3.3.1   Euler's Elastica

Before we develop our model, let's sketch Euler's Elastica. More details can be found in [Mum94, CKS02].

A curve Γ is said to be an *Euler's elastica* if it is the equilibrium curve of the elasticity energy:

$$E_2(\gamma) \;=\; \int_\gamma (a + b\kappa^2)ds, \qquad\qquad (3.5)$$

where ds denotes the arc length element, $\kappa(s)$ the scalar curvature and a, b are two positive parameters.

In a level set function based setting, that is, the curve γ is embedded as the zero level set of a function ϕ defined in the domain Ω, (3.5) can be rewritten as follows:

$$E_2(\phi) \;=\; \int_\Omega \{a + b[\nabla \cdot (\frac{\nabla\phi}{|\nabla\phi|})]^2\}|\nabla\phi|\delta(\phi)dxdy, \qquad\qquad (3.6)$$

where $\delta(x)$ is the Dirac function or the derivative of the Heaviside function:

$$H(x) \;=\; \begin{cases} 1, & \text{x}\geq 0 \\ 0, & \text{x}<0, \end{cases} \qquad\qquad (3.7)$$

in the distribution sense, and $|\nabla\phi|\delta(\phi)dxdy$ represents the arc length ds (see [OF01]).

3.3.2 The model

Let $u : \Omega \to R^1$ be an image defined on the domain Ω. Since we focus mainly on the problem of how to capture illusory contours, we consider in this chapter only binary images, i.e., u takes only two distinct values in Ω. Without loss of generality, let's assume that u takes the value 1 on the regions occupied by objects and the value -1 on the background. Then, by solving the steady state of the following Hamilton-Jacobi equation (Eikonal equation)(for instance, see [PMO99]):

$$\frac{\partial d}{\partial t} \;=\; \text{sign}(u)(1 - |\nabla d|), \tag{3.8}$$

with $d(x, 0) = u(x)$, we get the signed distance function according to the boundaries of the objects in the image, and the signed distance function is positive in the objects and negative on the background.

Let ϕ be the level set function whose zero level set locates the illusory contours. We develop our model as follows:

$$
\begin{aligned}
E(\phi) \;=\;& E_1(\phi) + E_2(\phi) \\
\;=\;& \int_\Omega [|d|\delta(\phi)|\nabla\phi| + \lambda H(d)H(\phi)]dxdy + \\
& \int_\Omega \{a + b[\nabla \cdot (\frac{\nabla\phi}{|\nabla\phi|})]^2\}|\nabla\phi|\delta(\phi)dxdy,
\end{aligned}
\tag{3.9}
$$

where $|d|$ means the absolute value of d, λ, a, b are nonnegative parameters, and $\delta(x)$ is the Dirac function.

In the model, minimizing the first energy $E_1(\phi)$ will derive the zero level set of ϕ to the inside desired boundaries of objects. Note that the term $\int_\Omega |d|\delta(\phi)|\nabla\phi|dxdy$ measures the sum of distances from points on the zero level set to objects' boundaries. And the term $\int_\Omega \lambda H(d)H(\phi)dxdy$ describes the area of objects inside the

32

region $\{(x, y) \in \Omega : \phi(x, y) > 0\}$. On the other hand, the second energy $E_2(\phi)$, Euler's elasticity energy, controls the smoothness of the zero level set as well as its length.

In contrast to $E_1(\phi)$, $E_2(\phi)$ is independent of image information, and only depends on the zero level set itself. It prevents the emergence of points with high curvatures, such as corners, along the curve. This property is reverse to what we want. For instance, in the case of Kanizsa triangle, it is crucial to preserve the corners to provide an excellent visual perception. Therefore, the above energy is insufficient to fulfill what we may expect.

We demonstrate the phenomenon in Figure 3.1. In this example, the three corners are all smeared while the missing boundaries are not straightened enough as what they are supposed to be. For this example, to preserve the three corners, we have to choose the two coefficients a, b in Euler's elasticity energy (3.6) as small as possible; on the other hand, we need to fortify them so that the missing boundaries can be straightened enough. How to overcome this dilemma?

To handle this *dilemma*, we would like to revise the first energy $E_1(\phi)$ such that the zero level set will stick to the boundaries especially those corners with high curvatures. A nature idea is to combine curvature information of *objects'* boundaries into $E_1(\phi)$.

Let's still use the classic illusory contour—Kanizsa triangle to illustrate how to incorporate curvature information of object's boundaries into $E_1(\phi)$. In Figure 3.2, we present a Kanizsa triangle. The point A is a "concave" point and B is a "convex" one. As in Figure 3.1, we see that all the concave points are smeared. This is because $E_2(\phi)$ is a dominating energy in the competition with $E_1(\phi)$
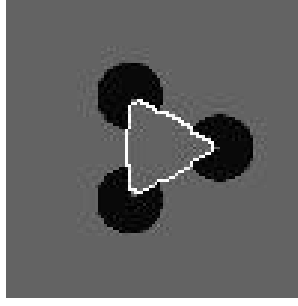
Figure 3.1: The white curve is the zero level set in the steady state by minimizing the functional (3.9). The three corners are all smeared (c.f. Figure 1.1(a)) while the missing boundaries are not straightened enough. This example shows that the energy (3.9) is insufficient to capture the illusory contours, especially for the ones with high curvature points such as corners.

near them. Therefore, we have to strengthen $E_1(\phi)$ to balance $E_2(\phi)$ near these concave points. On the other hand, for convex points, such as point B, we prefer small amount of $E_1(\phi)$ so that the zero level set of ϕ is controlled by $E_2(\phi)$. Hence, it is preferable to keep $E_1(\phi)$ near these convex points.

Due to the fact that the signed distance function $d(x,y)$ is positive inside the regions occupied by objects and negative on the background, we can discriminate concave points and convex points by the sign of the curvature at those points. Specifically, $\kappa(d) = \nabla \cdot (\nabla d / |\nabla d|)$ is positive at the concave point A, and negative at the convex point B. Consequently, we can use $\kappa^+(d) = max(\kappa(d), 0)$ to separate concave points and convex points.

Moreover, since we only need to revise $E_1(\phi)$ near the above corners, we introduce a cut-off function $C(x)$ which will be 1 in a tube around objects' boundaries, and be 0 else where.

34
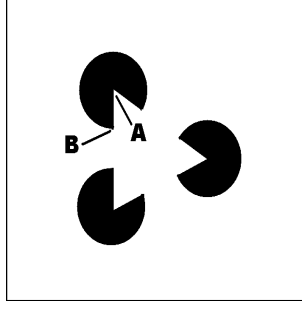
Figure 3.2: In this figure, the point A is a concave point where the curvature $\kappa(d)$ is positive, and the point B is a convex point at which the curvature $\kappa(d)$ is negative. Note that the function d is the signed distance function corresponding to objects' boundaries, and it is positive inside objects and negative on the background.

Consequently, we revise $E_1(\phi)$ as follows:

$$E_1(\phi) \;\; = \;\; \int_\Omega [(1 + \mu C(d)\kappa^+(d))|d|\delta(\phi)|\nabla\phi| + \lambda H(d)H(\phi)]dxdy, \quad (3.10)$$

where we may choose a C^1 cut-off function $C(x)$ as follows:

$$C(x) \;\; = \;\; \begin{cases} 1, & |x| \le \varepsilon; \\ (|x| - 2\varepsilon)^2(2|x| - \varepsilon)/\varepsilon^3, & \varepsilon < |x| \le 2\varepsilon; \\ 0, & |x| > 2\varepsilon, \end{cases} \quad (3.11)$$

where ϵ is a small constant, and $\mu > 0$ is a parameter.

Remark 1: We substitute the term $[1 + \mu C(d)\kappa^+(d)]|d|\delta(\phi)|$ for $|d|\delta(\phi)|\nabla\phi|$ in $E_1(\phi)$. It means that we impose more weight for concave points so that the strength for steering the zero level set to them is enforced. And the strength is proportional to the curvature at the concave points. In some sense, the revision of $E_1(\phi)$ is reasonable because it is these concave points that provide more vision cues for identifying the illusory contours.

35

In summary, our proposed functional reads:

$$
\begin{aligned}
E(\phi) &= E_1(\phi) + E_2(\phi) \\
&= \int_\Omega \{[(1 + \mu C(d)\kappa^+(d))|d|\delta(\phi)|\nabla\phi| + \lambda H(d)H(\phi)] \\
&\quad + [a + b(\nabla \cdot (\frac{\nabla\phi}{|\nabla\phi|}))^2]|\nabla\phi|\delta(\phi)\}dxdy.
\end{aligned}
\tag{3.12}
$$

3.3.3 Numerical Algorithms

In this section, we discuss the Euler-Lagrange equation about ϕ according to the functional (3.12) as well as the numerical algorithms.

To be clear, we consider $E_1(\phi)$ and $E_2(\phi)$ separately.

For $E_1(\phi)$, it is easily to get the Euler-Lagrange equation as:

$$
\begin{aligned}
\frac{\partial\phi}{\partial t} &= \delta(\phi)\{\nabla[(1 + \mu C(d)\kappa^+(d))|d|] \cdot \frac{\nabla\phi}{|\nabla\phi|} \\
&\quad + [1 + \mu C(d)\kappa^+(d)|d|]\nabla \cdot (\frac{\nabla\phi}{|\nabla\phi|}) - \lambda H(d)\}.
\end{aligned}
\tag{3.13}
$$

For $E_2(\phi)$, similar derivations for the Euler-Lagrange equation can be found in [CKS02]; we also discuss the details in the next Chapter. The equation reads:

$$
\frac{\partial\phi}{\partial t} = \delta(\phi)\nabla \cdot \vec{V},
\tag{3.14}
$$

where

$$
\vec{V} = \{(a + b\kappa^2)\vec{n} - \frac{2b}{|\nabla\phi|}\frac{\partial(\kappa|\nabla\phi|)}{\partial\vec{t}}\vec{t}\},
$$

and $\vec{n} = \nabla\phi/|\nabla\phi|$, $\vec{t} = (-\phi_y/|\nabla\phi|, \phi_x/|\nabla\phi|)$, $\kappa = \nabla \cdot (\nabla\phi/|\nabla\phi|)$.

Then, by combining (3.13) and (3.14) and replace $\delta(\phi)$ by $|\nabla\phi|$ as in [ZCM96] (the factor $|\nabla\phi|$ also helps to accelerate the evolution as discussed in [MO00]),

we have the gradient descent equation as follows:

$$
\begin{aligned}
\frac{\partial \phi}{\partial t} &= \nabla[(1 + \mu C(d)\kappa^+(d))|d|] \cdot \nabla \phi - \lambda H(d)|\nabla \phi| \\
&+ [1 + \mu C(d)\kappa^+(d)|d|]|\nabla \phi|\nabla \cdot (\frac{\nabla \phi}{|\nabla \phi|}) + |\nabla \phi|\nabla \cdot \vec{V}. \quad (3.15)
\end{aligned}
$$

In the experiments, we first calculate the signed distance function d by solving (3.8) with the standard method which can be found in Peng et al [PMO99] , then obtain the curvature $\kappa(d)$ and the gradient of $(1 + \mu C(d)\kappa^+(d))|d|$ at each grid point.

In the following, we discuss how to choose the discrete form for each term in the equation (3.15).

In fact, it is subtle to choose the discrete form of the first two terms. We follow the idea discussed in Osher and Fedkiw's book [OF02]. The key point is how to determine the value of ϕ_x and ϕ_y.

For simplicity, let's denote $A = (1 + \mu C(d)\kappa^+(d))|d|$.

Let

$$
H(\phi_x, \phi_y) = \nabla A \cdot \nabla \phi - \lambda H(d)|\nabla \phi|, \quad (3.16)
$$

then the partial derivatives to the two augments are:

$$
H_1(\phi_x, \phi_y) = A_x - \lambda H(d)\frac{\phi_x}{|\nabla \phi|}, \quad (3.17)
$$

$$
H_2(\phi_x, \phi_y) = A_y - \lambda H(d)\frac{\phi_y}{|\nabla \phi|}, \quad (3.18)
$$

where $A_x = \partial A/\partial x$, $A_y = \partial A/\partial y$. Since we do re-initialization for ϕ frequently in the experiments, we may assume $|\nabla \phi| = 1$, the above two derivatives can be

rewritten as:

$$H_1(\phi_x, \phi_y) \;=\; A_x - \lambda H(d)\phi_x, \qquad\qquad (3.19)$$

$$H_2(\phi_x, \phi_y) \;=\; A_y - \lambda H(d)\phi_y, \qquad\qquad (3.20)$$

To determine the values of ϕ_x and ϕ_y, we set $\phi_x^+ = (\phi_{i+1,j} - \phi_{i+1,j})/h$ and $\phi_x^- = (\phi_{i,j} - \phi_{i-1,j})/h$. Then we check the following cases:

- Case 1. $H(d) > 0$

  - 1. if $H_1(\phi_x^+, \phi_y) > 0$, $H_1(\phi_x^+, \phi_y) > 0$, then $\phi_x = \phi_x^-$,

  - 2. if $H_1(\phi_x^+, \phi_y) < 0$, $H_1(\phi_x^+, \phi_y) > 0$, then $\phi_x = A_x/(\lambda H(d))$,

  - 3. if $H_1(\phi_x^+, \phi_y) > 0$, $H_1(\phi_x^+, \phi_y) < 0$, then

    * 3a. $\phi_x^- \le \phi_x^+$,

      if $H_1(\phi_x^-, \phi_y) < H_1(\phi_x^+, \phi_y)$, then $\phi_x = \phi_x^-$, else $\phi_x = \phi_x^+$,

    * 3b. $\phi_x^- > \phi_x^+$,

      if $H_1(\phi_x^-, \phi_y) < H_1(\phi_x^+, \phi_y)$, then $\phi_x = \phi_x^+$, else $\phi_x = \phi_x^-$,

  - 4. if $H_1(\phi_x^+, \phi_y) < 0$, $H_1(\phi_x^+, \phi_y) < 0$, then $\phi_x = \phi_x^+$,

- Case 2. $H(d) = 0$

  - 1. if $A_x > 0$, then $\phi_x = \phi_x^+$,

  - 2. if $A_x \le 0$, then $\phi_x = \phi_x^-$.

Similarly, we can chose the value ϕ_y according to the same principle.

For the third term, we use the central difference, that is,

$$\phi_{xx} \approx \frac{\phi_{i+1,j} - 2\phi_{i,j} + \phi_{i-1,j}}{h^2},$$

$$\phi_{yy} \approx \frac{\phi_{i,j+1} - 2\phi_{i,j} + \phi_{i,j-1}}{h^2},$$

$$\phi_{xy} \approx \frac{\phi_{i+1,j+1} + \phi_{i-1,j-1} - \phi_{i+1,j-1} + \phi_{i-1,j+1}}{4h^2},$$

and

$$\phi_x \approx \frac{\phi_{i+1,j} - \phi_{i-1,j}}{2h},$$

$$\phi_y \approx \frac{\phi_{i,j+1} - \phi_{i,j-1}}{2h}$$

to approximate

$$\kappa(\phi)|\nabla\phi| = \frac{\phi_x^2 \phi_{yy} - 2\phi_x \phi_y \phi_{xy} + \phi_y^2 \phi_{xx}}{\phi_x^2 + \phi_y^2}.$$

For the last term, details can be found in [CKS02].

Since the zero level set of ϕ is the only thing that we want, we employ a local level set method [PMO99] to solve (3.15) to reduce the computations. The point is: instead of solving the following equation:

$$\frac{\partial \phi}{\partial t} + u_n |\nabla \phi| = 0, \tag{3.21}$$

they solve

$$\frac{\partial \phi}{\partial t} + c(\phi) u_n |\nabla \phi| = 0, \tag{3.22}$$

where

$$c(x) = \begin{cases} 1, & |x| \leq \beta; \\ (|x| - \gamma)^2 (2|x| + \gamma - 3\beta)/(\gamma - \beta)^3, & \beta < |x| \leq \gamma; \\ 0, & |x| > \gamma, \end{cases} \tag{3.23}$$

where β and γ are two positive constants. In the experiments, we choose $\beta = 3h$, $\gamma = 6h$, and h is the spatial mesh size.

Remark 2. This local level set method speeds up the evolution process remarkably, since it only updates the level set function ϕ inside a tube around its zero level set. It changes a two-dimensional problem into a one-dimensional one in some sense. In fact, it is necessary to utilize this method. Note that the evolution equation (3.15) is actually a fourth-order one if the parameter $b \neq 0$, therefore by the CFL condition, the time step size should be proportional to the fourth power of the spatial step size, i.e., $dt \sim dx^4$.

Remark 3. The employment of the local level set method is also crucial. In [CS99], Chopp and Sethian discussed the case of curvature flow as well as the flow under Laplacian of curvature. In the case of curvature flow, the level sets behave nicely and any two different level sets will not cross. However, the situation will become totally different for the flow under Laplacian of curvature: two different level sets may intersect; one level set could collide with itself; and even zero level sets could emerge automatically. Fortunately, the local level set method may prevent the possibility that other zero level sets emerge and intersect with the goal zero level. On the other hand, the situation that the goal zero level set collides with itself can be excluded because of the term of Euler's elastica.

3.4 Numerical Experiments

In this section, we present some examples including Kanizsa triangle and square as well as many synthetic ones.

For all the experiments listed here, the images are all 100×100, and defined on $[-4, 4] \times [-4, 4]$. Basically, it takes less than $10^3 \sim 10^4$ iterations when the missing parts are straight lines, i.e., $b = 0$, and $10^6 \sim 10^7$ iterations for the curved

cases where $b \neq 0$. Moreover, we may choose the initialization of ϕ freely— we only require its zero level set contains all the objects in the image.

Figures 3.3 and 3.4 show the classical illusory contours—Kanizsa triangle and square. In these two examples, we only need to choose $b = 0$ in (3.15) because the missing boundaries are actually straight lines by the continuity of curvature; on the other hand, a nonzero choice of b will not affect the final results. The choice of $b = 0$ makes the evolution equation (3.15) become a second order instead of fourth order equation, which accelerates the evolution process remarkably. In these two examples, the corners are preserved very well while the missing contours are integrated by straight lines automatically.

Figure 3.5 is a general four-edged illusory contour. As in Figure 3.3 and 3.4, we also choose $b = 0$ in (3.15). As the previous examples, the corners are preserved very well.

The above three examples verify that our model can be applied to the cases that the missing boundaries are straight lines. As described in the model, on one hand, the zero level set of the goal function is steering to the objects' boundaries; on the other hand, it also sticks to the corners, which helps to provide good vision perception.

The next three examples (Figure 3.6, Figure 3.7, and Figure 3.8) demonstrate that our model is also capable of completing missing boundaries by curves. We choose nonzero b in (3.15) here. As in the previous examples, the zero level set is driven to the desirable objects' boundaries, and it completes the missing boundaries by short smooth curves along which there are no salient jumps of curvature.

Figure 3.3: This image is the classical Kanizsa Triangle. The evolution process is listed with four figures from left to right. The parameters chosen for this example are: $\lambda = 3.0$, $\mu = 15.0$, $a = 0.5$, $b = 0$.
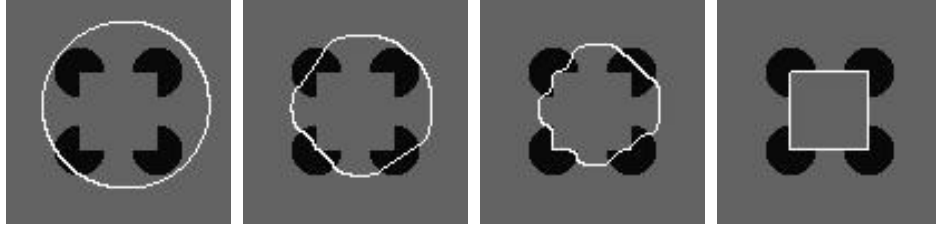
Figure 3.4: This image is the classical Kanizsa Square. The evolution process is listed with four figures from left to right. The parameters chosen for this example are: $\lambda = 3.0$, $\mu = 15.0$, $a = 0.5$, $b = 0$.

In Figure 3.9, we present the result by choosing $b = 0$. One may find the missing boundaries are completed by straight lines, instead of smooth curves as in Figure 3.6. This shows the Euler's Elastica does preserve the continuity of curvature.

In Figure 3.10, we present a group of results for the same image with different choice of the parameter b. We find that with the same choice of the parameter a, the larger the parameter b, the less the change rate of the curvature along the missing parts.

Figure 3.5: This image is a general four-edged shape. The evolution process is listed with four figures from left to right. The parameters chosen for this example are: $\lambda = 3.0$, $\mu = 15.0$, $a = 0.5$, $b = 0$.
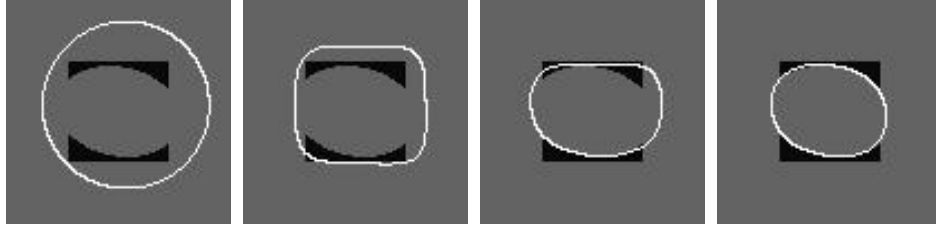
Figure 3.6: This image contains an illusory ellipse inside a square. The evolution process is listed with four figures from left to right. The parameters chosen for this example are: $\lambda = 3.0$, $\mu = 15.0$, $a = 0.01$, $b = 0.5$.

In the last examples (Figure 3.11), we list a comparison for some illusory contours with or without real junctions. We can see that the presence of real junctions helps to capture the desirable illusory contours. It therefore supports the fact that the junctions are crucial to recognize illusory contours. Moreover, it also supports our postulation in the last Chapter that shape information has a role to play in capturing illusory contours, especially for those without real junctions.

Figure 3.7: In this image, the illusory contour is a dumb-bell. The evolution process is listed with four figures from left to right. The parameters chosen for this example are: $\lambda = 3.0$, $\mu = 15.0$, $a = 0.005$, $b = 0.05$.
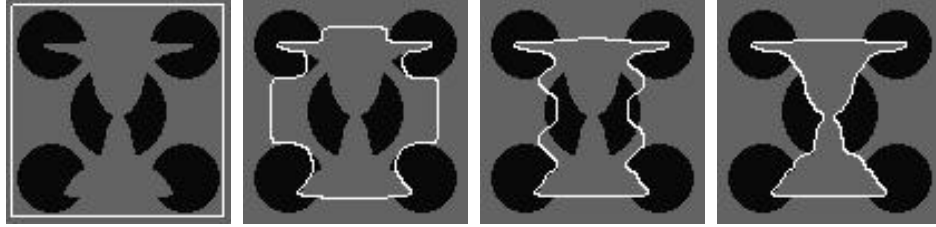
Figure 3.8: In this image, the illusory contour is a Rubin Vase(or two faces). The evolution process is listed with four figures from left to right. The parameters chosen for this example are: $\lambda = 3.0$, $\mu = 60.0$, $a = 0.1$, $b = 0.01$.

3.5 Conclusion

In this chapter, we propose a level set based variational model to capture illusory contours by incorporating objects' curvature information. Our model employs Euler's elastica to complete the missing boundaries in a smooth way, and preserves real junctions very well. It is thus capable of a wide range of illusory contours regardless of straight lines or curves as the missing boundaries.
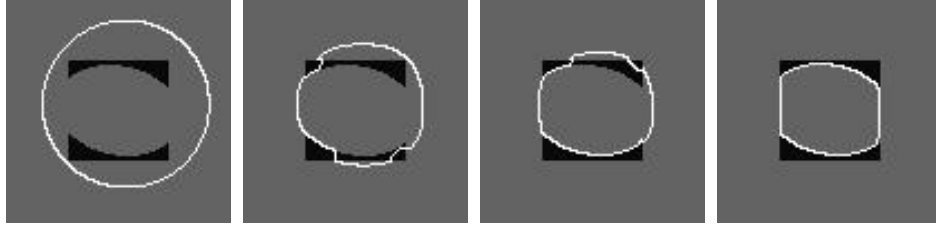
Figure 3.9: This image is an ellipse inside a square. The evolution process is listed with four figures from left to right. The parameters chosen for this example are: $\lambda = 3.0$, $\mu = 15.0$, $a = 0.01$, $b = 0$.
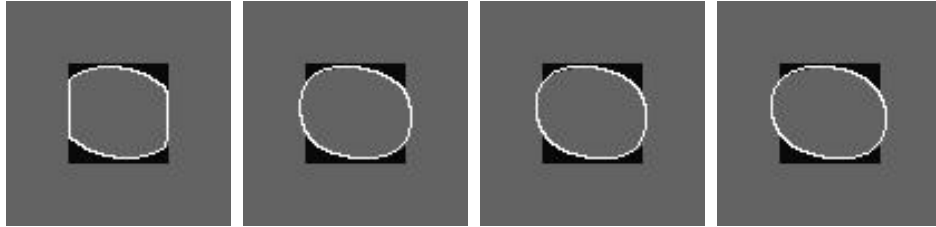
Figure 3.10: These images are the final results according to different choices of the parameter b and the same a. Here $a = 0.01$, and $b = 0, 0.1, 0.3, 0.5$ from left to right respectively.
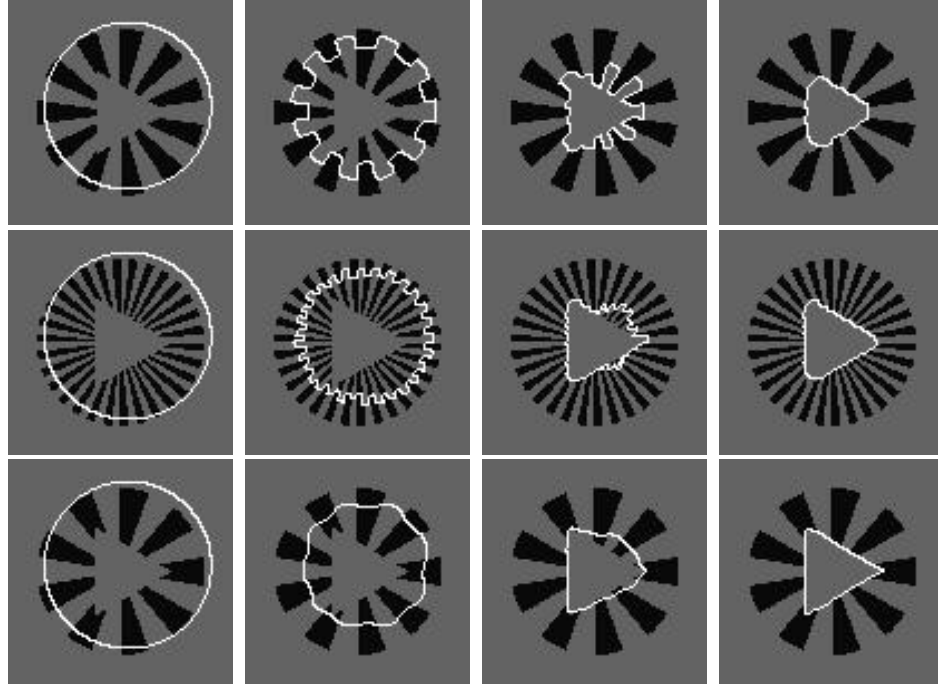
Figure 3.11: The comparison for the illusory contours with or without real junctions. We can see that our model yields a good result for the example in the third row, since the real junctions are present for this case, but fails for the other two cases without real junctions. It supports the fact that the junctions are crucial to recognize illusory contours.

CHAPTER 4

A level set approach to segmentation with depth

4.1 Introduction

In this chapter, we employ level set methods [OS88] to numerically minimize the Nitzberg-Mumford-Shiota functional on segmentation with depth [NMS93]. Segmentation with depth is different from standard segmentation which only depends on the gray intensity distributions in image domains (see Figure 4.1). Segmentation with depth also takes into account the orderings among objects, i.e., it allows the occlusions between objects. Therefore, in the process of segmentation with depth, boundaries are determined by the gray intensity distribution as well as the ordering among objects. For instance, if a farther object is blocked by other ones that are nearer, a reconstruction of its occluded boundaries is needed in segmentation with depth.

In [NMS93], Nitzberg, Mumford, and Shiota proposed a variational model to the segmentation with depth problem. Their model provides a principle to reconstruct the occluded boundaries by employing curvature information along objects' boundaries, and thus determines the ordering of objects by comparing each energy corresponding to each ordering assumption. To minimize the prescribed functional, the authors introduce a combinatoric method, i.e., they first compute

Front   Behind
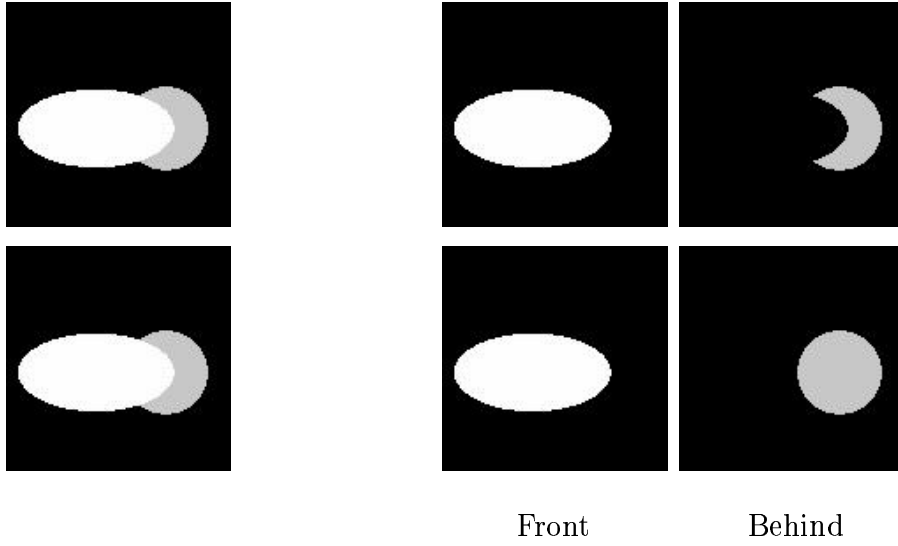
Figure 4.1: The first row contains the original image (Left) with two regions (middle and right) given by any multi-phase gray intensity based segmentation method, and the second row illustrates the results from a segmentation with depth model. Besides the occlusion relation between the two objects ("Front" and "Behind" in this example), the missing boundary of the behind object is also restored.

edges and T-junctions, and then minimize the functional according to each assumption of objects' ordering by using the T-junctions. In [EM03], Esedoglu and March provide a new numerical technique for the minimization problem of the Nitzberg-Mumford-Shiota functional. Their algorithm is based on regions or the associated boundaries evolving. However, it is difficult to handle the curvature terms in the above functional. Esedoglu and March took advantage of the notion of $\Gamma-$ convergence, which was introduced by Degorgi [Gio91], to approximate the curvature terms by more manageable ones. Even though, they still could not approximate the primitive curvature terms, which involve absolute values of curvatures, in the Nitzberg-Mumford-Shiota functional, and they instead choose

48

the quadratic form of curvature.

In this chapter, we utilize level set method [OS88] to minimize the Nitzberg-Mumford-Shiota functional, since it is easy to handle the curvature terms. For instance, let ϕ be a level set function, then the curvature κ along any level curves $\phi = c$ (c is any real value) can be represented as:

$$\kappa \quad = \quad \nabla \cdot (\frac{\nabla \phi}{|\nabla \phi|}). \tag{4.1}$$

With the representation, it is also trivial to handle the absolute value of curvature that appears in the above functional. By using level set methods, the problem of minimizing the Nitzberg-Mumford-Shiota functional turns out to be solving a system of fourth order partial differential equations. This kind of equations was also solved in the last chapter for capturing illusory contours. Moreover, we employ Smereka's semi-implicit method [Sme03] to solve the associated fourth order equations. This method can speed up the convergence process, since conventional methods for these equations are notorious slow to arrive at the convergent states.

The remain of this chapter is organized as follows. In the next section, we introduce the background of segmentation with depth as well as the Nitzberg-Mumford-Shiota functional. In section 4.3, we rewrite the functional in a level set based setting and derive the associated Euler-Lagrange equations. And we continue to talk about the numerics including Smereka's semi-implicit method in the subsequent section 4.4. In section 4.5, we present some numerical experiments on synthetic images that appears in [EM03]. In section 4.6, we make a conclusion.

4.2 Nitzberg-Mumford-Shiota functional

In this section, we sketch the problem of segmentation with depth and present the Nitzberg-Mumford-Shiota functional. More details can be found in [NMS93, EM03].

Briefly, segmentation with depth is to determine the ordering of objects in space as well as their boundaries in a given 2-D gray scale image. The ordering of objects refers to the position that one object is farther or nearer an observer than the others. Due to the permission of occlusions between objects, farther objects always consist of two parts: visible and invisible parts. The visible parts are determined by the gray intensity distribution, while the invisible parts should be reconstructed by following some principle. In Nitzberg-Mumford-Shiota's model, they reconstruct invisible parts of regions by using curvature information along the boundaries.

Let $f : \Omega \rightarrow R^1$ be a 2-D image defined on $\Omega \subset R^2$, and $R_1, ..., R_n$ be the regions occupied by objects inside the image. Denote the visible parts of the above objects by $R_1^{'}, ..., R_n^{'}$ respectively.

To simplify the problem, we make some assumptions as follows:

- each object does not entangle with itself.

- any two objects do not entangle with each other.

- the intensity in the region occupied by any object is uniform.

With these assumptions, two questions related to the problem of segmentation with depth are:

- How to determine the ordering among the objects? In fact, there will be $n!$ cases of ordering.

- How to reconstruct the invisible regions(boundaries) of farther objects that are occluded by nearer ones?

In [NMS93], the authors propose a functional, and calculate its value for each case of the ordering. Then they claim that the ordering associated to the smallest value of the functional is the desirable ordering. Moreover, the reconstruction of visible regions is automatically accomplished during the calculation of the functional for each ordering.

Suppose the regions $R_1, ..., R_n$ are listed in the increasing farther order in the given image, i.e., R_1, R_n are the nearest and farthest regions respectively. Then the visible part R'_i of R_i is given by:

$$R'_1 = R_1, \quad R'_i = R_i - \bigcup_{j<i} R_j, \quad \text{for } i = 2, ..., n.$$

For simplicity, we denote by $R'_{n+1} = \Omega - \bigcup_{j<n+1} R_j$ as the background. Then the Nitzberg-Mumford-Shiota functional reads:

$$E = \sum_{i=1}^{n} \int_{\partial R_i \cap \Omega} [\alpha + \beta\phi(\kappa)]ds + \sum_{i=1}^{n+1} \int_{R'_i} (f(x) - c_i)^2 dx, \qquad (4.2)$$

where α, β are two nonnegative parameters, and the unknown $c_i \in R^1$ is the intensities in R_i, $i = 1, ..., n+1$. The function ϕ determines how the curvature information will be incorporated in the functional. The authors choose ϕ as follows:

$$\phi(x) = \begin{cases} x^2, & |x| \text{ small}, \\ |x|, & \text{otherwise}. \end{cases} \qquad (4.3)$$

It is this choice of the function ϕ that allows corners along objects' boundaries.

Due to the permission of occlusions between objects, in the functional (4.2), the first sum takes into account ∂R_i's inside Ω, instead of $\partial R_i'$'s which are the boundaries of visible parts of R_i's, while the second sum is a fitting term as that of standard segmentation models, for instance, Chan-Vese's segmentation model [CV01].

4.3 Level set method for minimizing the Nitzberg-Mumford-Shiota functional

As discussed in the section of introduction, it is very convenient to represent curvature of contours by using level set method. In this section, we first rewrite the Nitzberg-Mumford-Shiota functional (4.2) into a level set based formulation, then drive the associated Euler-Lagrange equations.

4.3.1 Level set formulation

Since each of the regions R_i's will evolve during the minimization process of (4.2), we assign for each of them a level set function. Let ψ_i be the level set function related to the region R_i, and we always require $R_i = \{\psi_i > 0\}$, $i = 1, ..., n$.

Then, the first sum of (4.2) can be rewritten as follows:

$$\sum_{i=1}^{n} \int_{\Omega} [\alpha + \beta\phi(\kappa_i)]|\nabla\psi_i|\delta(\psi_i)dx, \tag{4.4}$$

where $\kappa_i = \nabla \cdot \left(\frac{\nabla\psi_i}{|\nabla\psi_i|}\right)$ is the curvature of any level curve.

On the other hand, since $R_i' = R_i - \bigcup_{j<i} R_j$, and $R_i' = \{\psi_i > 0\} \bigcap (\bigcup_{j<i}\{\psi_j \leq$

0\}$), we may rewrite the second sum of (4.2) as follows:

$$\sum_{i=1}^{n} \int_{\Omega} (f - c_i)^2 H(\psi_i) \prod_{j=1}^{j=i-1} (1 - H(\psi_j)) dx + \int_{\Omega} (f - c_{n+1})^2 \prod_{j=1}^{j=n} (1 - H(\psi_j)) dx, \quad (4.5)$$

where H is the Heaviside function:

$$H(x) = \begin{cases} 1, & x > 0, \\ 0, & x \leq 0. \end{cases} \quad (4.6)$$

Combining (4.4) and (4.5), we obtain the Nitzberg-Mumford-Shiota functional in a level set based formulation as follows:

$$\begin{aligned} E &= \sum_{i=1}^{n} \int_{\Omega} [\alpha + \beta \phi(\kappa_i)] |\nabla \psi_i| \delta(\psi_i) dx \\ &+ \sum_{i=1}^{n} \int_{\Omega} (f - c_i)^2 H(\psi_i) \prod_{j=1}^{j=i-1} (1 - H(\psi_j)) dx \\ &+ \int_{\Omega} (f - c_{n+1})^2 \prod_{j=1}^{j=n} (1 - H(\psi_j)) dx, \end{aligned} \quad (4.7)$$

4.3.2 Derivation of the Euler-Lagrange equations

To derive the associated Euler-Lagrange equations of the functional (4.7), we here only consider the terms that involve curvature, since the fidelity terms are easy to handle. For simplicity, let's consider a functional $\widehat{E}(\psi) = \int_{\Omega} \Phi(\kappa_\psi) |\nabla \psi| \delta(\psi) dx$, where $\Phi(x) = \alpha + \beta \phi(x)$ in the functional (4.7).

Before deriving the Euler-Lagrange equation of ψ according to the minimization of $\widehat{E}(\psi)$, let's notice two simple facts.

Lemma 1. Let $\overrightarrow{n} \in R^2$ be a unit vector, and $I, P_{\overrightarrow{n}} : R^2 \to R^2$ be two operators with $I(\overrightarrow{v}) = \overrightarrow{v}$, $P_{\overrightarrow{n}}(\overrightarrow{v}) = (\overrightarrow{v} \cdot \overrightarrow{n}) \overrightarrow{n}$, for any $\overrightarrow{v} \in R^2$. Then for the curvature $\kappa = \nabla \cdot (\frac{\nabla \psi}{|\nabla \psi|})$, we have $\frac{\partial \kappa}{\partial t} = \nabla \cdot ((I - P_{\overrightarrow{n}}) \frac{\nabla \psi_t}{|\nabla \psi|})$, where $\overrightarrow{n} = \frac{\nabla \psi}{|\nabla \psi|}$.

Proof. Simple calculation shows the conclusion. $\qquad\square$

Lemma 2. *With the same notation as in lemma 1, we have* $(I - P_{\overrightarrow{n}})\overrightarrow{v} \cdot \overrightarrow{w} = (I - P_{\overrightarrow{n}})\overrightarrow{w} \cdot \overrightarrow{v}$, *for any* $\overrightarrow{v}, \overrightarrow{w} \in R^2$.

We may thus obtain the following theorem.

Theorem 1. *Let* $\widehat{E}(\psi) = \int_\Omega \Phi(\kappa)|\nabla\psi|\delta(\psi)dx$, *then the associated Euler-Lagrange equation reads:* $(P = P_{\frac{\nabla\psi}{|\nabla\psi|}}.)$

$$\frac{\partial\psi}{\partial t} = |\nabla\psi|\nabla\cdot[\frac{\nabla\psi}{|\nabla\psi|}\Psi(\kappa) - \frac{1}{|\nabla\psi|}(I - P)(\nabla(\Psi'(\kappa)|\nabla\psi|))]. \qquad (4.8)$$

Proof. To get the Euler-Lagrange equation, let's take the derivative of $\widehat{E}$ according to time t, then determine the derivative of ψ to t by decreasing the functional $\widehat{E}$.

In fact,

$$
\begin{aligned}
\frac{d\widehat{E}}{dt} &= \int_\Omega \Psi'(\kappa)\kappa_t|\nabla\psi|\delta(\psi) + \Psi(\kappa)|\nabla(\psi)|_t\delta(\psi) + \Psi(\kappa)|\nabla(\psi)|\delta'(\psi)\psi_t \\
&= \int_\Omega \Psi'(\kappa)\nabla\cdot[(I-P)(\frac{\nabla\psi_t}{|\nabla\psi|})]|\nabla\psi|\delta(\psi) + \Psi(\kappa)\nabla\psi_t\cdot\frac{\nabla\psi}{|\nabla\psi|}\delta(\psi) \\
&\quad + \int_\Omega \Psi(\kappa)|\nabla(\psi)|\delta'(\psi)\psi_t \\
&= \int_\Omega \nabla\cdot[(I-P)(\frac{\nabla\psi_t}{|\nabla\psi|})\Psi'(\kappa)|\nabla\psi|\delta(\psi)] + \int_\Omega \nabla\cdot[\psi_t\frac{\nabla\psi}{|\nabla\psi|}\Psi(\kappa)\delta(\psi)] \\
&\quad - \int_\Omega (I-P)(\frac{\nabla\psi_t}{|\nabla\psi|})\cdot\nabla(\Psi'(\kappa)|\nabla\psi|\delta(\psi)) - \psi_t\nabla\cdot[\frac{\nabla\psi}{|\nabla\psi|}\Psi(\kappa)\delta(\psi)] \\
&\quad + \int_\Omega \Psi(\kappa)|\nabla(\psi)|\delta'(\psi)\psi_t, \qquad\qquad (4.9)
\end{aligned}
$$

so, if we choose Neunman boundary conditions, we may drop the two divergence

54

terms, and get

$$
\begin{aligned}
\frac{d\widehat{E}}{dt} &= \int_\Omega -(I-P)(\frac{\nabla \psi_t}{|\nabla \psi|}) \cdot \nabla(\Psi^{'}(\kappa)|\nabla \psi|\delta(\psi)) \\
&\quad - \int_\Omega \psi_t \nabla \cdot [\frac{\nabla \psi}{|\nabla \psi|}\Psi(\kappa)\delta(\psi)] + \Psi(\kappa)|\nabla(\psi)|\delta^{'}(\psi)\psi_t, \qquad (4.10)
\end{aligned}
$$

by lemma 2, $(I-P)\overrightarrow{v} \cdot \overrightarrow{w} = \overrightarrow{v} \cdot (I-P)\overrightarrow{w}$, we have

$$
\begin{aligned}
\frac{d\widehat{E}}{dt} &= \int_\Omega -\frac{\nabla \psi_t}{|\nabla \psi|} \cdot (I-P)[\nabla(\Psi^{'}(\kappa)|\nabla \psi|\delta(\psi)] \\
&\quad -\psi_t \nabla \cdot [\frac{\nabla \psi}{|\nabla \psi|}\Psi(\kappa)\delta(\psi)] + \int_\Omega \Psi(\kappa)|\nabla(\psi)|\delta^{'}(\psi)\psi_t \\
&= \int_\Omega -\nabla \cdot [\psi_t \frac{1}{|\nabla \psi|}(I-P)(\nabla(\Psi^{'}(\kappa)|\nabla \psi|\delta(\psi)))] \\
&\quad +\psi_t \nabla \cdot [\frac{1}{|\nabla \psi|}(I-P)(\nabla(\Psi^{'}(\kappa)|\nabla \psi|\delta(\psi)))] \\
&\quad - \int_\Omega \psi_t[\nabla \cdot (\frac{\nabla \psi}{|\nabla \psi|}\Psi(\kappa))\delta(\psi) + \frac{\nabla \psi}{|\nabla \psi|}\Psi(\kappa) \cdot \delta^{'}(\psi)\nabla(\psi)] \\
&\quad + \int_\Omega \Psi(\kappa)|\nabla(\psi)|\delta^{'}(\psi)\psi_t, \qquad (4.11)
\end{aligned}
$$

Notice that $\nabla(\Psi^{'}(\kappa)|\nabla \psi|\delta(\psi)) = \nabla(\Psi^{'}(\kappa)|\nabla \psi|)\delta(\psi) + \Psi^{'}(\kappa)|\nabla \psi|\delta^{'}(\psi)\nabla \psi$, then $(I-P)\nabla(\Psi^{'}(\kappa)|\nabla \psi|\delta(\psi)) = (I-P)\nabla(\Psi^{'}(\kappa)|\nabla \psi|)\delta(\psi)$, since $(I-P)\nabla \psi = 0$. Therefore, by dropping the divergence part in (4.11), we arrive at

$$
\begin{aligned}
\frac{d\widehat{E}}{dt} &= \int_\Omega \psi_t \nabla \cdot [\frac{1}{|\nabla \psi|}(I-P)(\nabla(\Psi^{'}(\kappa)|\nabla \psi|)\delta(\psi)] - \int_\Omega \psi_t \nabla \cdot [\frac{\nabla \psi}{|\nabla \psi|}\Psi(\kappa)]\delta(\psi) \\
&= \int_\Omega \psi_t\{\nabla \cdot [\frac{1}{|\nabla \psi|}(I-P)(\nabla(\Psi^{'}(\kappa)|\nabla \psi|)]\delta(\psi) \\
&\quad +\frac{1}{|\nabla \psi|}(I-P)(\nabla(\Psi^{'}(\kappa)|\nabla \psi|) \cdot \delta^{'}(\psi)\nabla \psi\} - \int_\Omega \psi_t \nabla \cdot [\frac{\nabla \psi}{|\nabla \psi|}\Psi(\kappa)]\delta(\psi) \\
&= \int_\Omega \psi_t \delta(\psi) \nabla \cdot [\frac{1}{|\nabla \psi|}(I-P)(\nabla(\Psi^{'}(\kappa)|\nabla \psi|) - \frac{\nabla \psi}{|\nabla \psi|}\Psi(\kappa)] \qquad (4.12)
\end{aligned}
$$

Therefore, if we choose $\psi_t = -\delta(\psi)\nabla \cdot [\frac{1}{|\nabla \psi|}(I-P)(\nabla(\Psi^{'}(\kappa)|\nabla \psi|)) - \frac{\nabla \psi}{|\nabla \psi|}\Psi(\kappa)]$, we see $\frac{d\widehat{E}}{dt} \leq 0$. Moreover, by employing the standard technique which replaces

$\delta(\psi)$ by $|\nabla\psi|$ (see [ZCM96]) , we then have the associated Euler-Lagrange equation:

$$\frac{\partial\psi}{\partial t} = |\nabla\psi|\nabla\cdot[\frac{\nabla\psi}{|\nabla\psi|}\Psi(\kappa) - \frac{1}{|\nabla\psi|}(I-P)(\nabla(\Psi'(\kappa)|\nabla\psi|))]. \quad (4.13)$$

$\square$

Let's turn to the original Nitzberg-Mumford-Shiota functional (4.7). From Theorem 1, the system of Euler-Lagrange equations reads:

$$\begin{aligned}
\frac{\partial\psi_i}{\partial t} &= |\nabla\psi_i|\nabla\cdot[\frac{\nabla\psi_i}{|\nabla\psi_i|}\Psi(\kappa_i) - \frac{1}{|\nabla\psi_i|}(I-P_{\frac{\nabla\psi_i}{|\nabla\psi_i|}})(\nabla(\Psi'(\kappa_i)|\nabla\psi_i|))] \\
&\quad +|\nabla\psi_i|(f-c_i)^2\prod_{j=1}^{i-1}(1-H(\psi_j)) \\
&\quad +|\nabla\psi_i|\sum_{j=i+1}^{n+1}[(f-c_s)^2H(\psi_s)\prod_{j=1}^{i-1}(1-H(\psi_j))\prod_{j=i+1}^{s-1}(1-H(\psi_j))], \\
&\qquad\qquad\qquad i = 1,...,n, \quad (4.14)
\end{aligned}$$

where $\kappa_i = \nabla\cdot(\frac{\nabla\psi_i}{|\nabla\psi_i|})$, and $H(\psi_{n+1}) = 0$.

4.4   Numerical Implementation

In this section, we show how to discretize each term in the equations (4.14) and explain how to apply Smereka's Semi-Implicit method to solve the equations.

4.4.1   Discretization of the Euler-Lagrange equations

We first discuss the schemes for the fourth order terms in (4.14). For clarity, we rewrite them as follow:

$$\frac{\partial\phi}{\partial t} = |\nabla\phi|\nabla\cdot\vec{V}, \quad (4.15)$$

where $\vec{V} = (V_1, V_2) = \frac{\nabla\phi}{|\nabla\phi|}\Psi(\kappa) - \frac{1}{|\nabla\phi|}(I - P)(\nabla(\Psi'(\kappa)|\nabla\phi|))$.

Then, denote $\Psi'(\kappa)|\nabla\psi|$ simply by A, we get:

$$V_1 = \Psi(\kappa)\frac{\psi_x}{|\nabla\psi|} - \frac{\psi_y}{|\nabla\psi|^3}[A_x\psi_y - A_y\psi_x], \qquad (4.16)$$

and

$$V_2 = \Psi(\kappa)\frac{\psi_y}{|\nabla\psi|} - \frac{\psi_x}{|\nabla\psi|^3}[A_y\psi_x - A_x\psi_y], \qquad (4.17)$$

where $A_x = \partial A/\partial x$, $A_y = \partial A/\partial y$.

Let (i, j) denote the pixel locations, h be the spatial step size and the time be discretized to be $\{ndt\}$, where $n = 0, 1, 2, ...$, and dt is the time step. Then $\psi_{i,j}^n$ refers to the value of ψ at pixel (i, j) at time ndt.

Let's discuss the disretization of each term in (4.15$\sim$ 4.17). In (4.15), we approximate $|\nabla\psi|$ by central difference as:

$$|\nabla\psi|_{i,j} = \sqrt{[\frac{\psi_{(i+1,j)} - \psi_{(i-1,j)}}{2h}]^2 + [\frac{\psi_{(i,j+1)} - \psi_{(i,j-1)}}{2h}]^2}, \qquad (4.18)$$

As for the terms in (4.16, 4.17), since

$$\begin{aligned}
\nabla \cdot \vec{V}_{(i,j)} &= V_{1x(i,j)} + V_{2y(i,j)} \\
&= \frac{V_{1(i+1/2,j)} - V_{1(i-1/2,j)}}{h} + \frac{V_{2(i,j+1/2)} - V_{2(i,j-1/2)}}{h}, \qquad (4.19)
\end{aligned}$$

we need to calculate the values of V_1 at the x-half-pixel $(i + 1/2, j)$, while the values of V_2 at the y-half-pixel $(i, j + 1/2)$.

We approximate the terms in (4.16) at $(i+1/2, j)$ as follows:

$$
\begin{aligned}
\kappa &= \operatorname{minmod}(\kappa_{(i,j)}, \kappa_{(i,j)}), \\
\psi_x &= \frac{\psi_{(i+1,j)} - \psi_{(i,j)}}{h}, \\
\psi_y &= \operatorname{minmod}(\frac{\psi_{(i+1,j+1)} - \psi_{(i+1,j-1)}}{2h}, \frac{\psi_{(i,j+1)} - \psi_{i,j-1}}{2h}), \\
|\nabla \psi| &= \sqrt{\psi_x^2 + \psi_y^2}, \\
A_x &= \frac{A_{(i+1,j)} - A_{(i,j)}}{h}, \\
&= \frac{\Psi'(\kappa_{(i+1,j)})|\nabla\psi|_{(i+1,j)} - \Psi'(\kappa_{(i,j)})|\nabla\psi|_{(i,j)}}{h}, \\
A_y &= \operatorname{minmod}(\frac{\Psi'(\kappa_{(i+1,j+1)})|\nabla\psi|_{(i+1,j+1)} - \Psi'(\kappa_{(i+1,j-1)})|\nabla\psi|_{(i+1,j-1)}}{2h}, \\
&\quad \frac{\Psi'(\kappa_{(i,j+1)})|\nabla\psi|_{(i,j+1)} - \Psi'(\kappa_{(i,j+1)})|\nabla\psi|_{(i,j-1)}}{2h}),
\end{aligned}
\tag{4.20}
$$

where

$$
\operatorname{minmod}(x, y) = \frac{\operatorname{sgn}(x) + \operatorname{sgn}(y)}{2} \min(|x|, |y|).
$$

Similarly, we may approximate the terms in (4.17).

As for the remain terms in (4.14), it should be careful to approximate $|\nabla\psi|$ (see Chapter 6 in [OF02]). Basically, we use the same technique as what we used in the last chapter, and we thus omit it here. And we approximate the Heaviside function $H(x)$ by a standard regularized function as follows:

$$
H_\epsilon(x) = \frac{1}{2}(1 + \frac{2}{\pi}\arctan(\frac{x}{\epsilon})),
$$

where ϵ is a fixed small number. In the experiments, we choose ϵ very small, for instance dx^2.

4.4.2 Smereka's Semi-Implicit method

Notice the equations (4.14) are fourth order equations, then CFL condition generally requires that the time step size dt is proportional to the fourth power of the spatial step size dx, i.e., $dt \sim dx^4$. This restriction will result in an intolerable long time for the minimization process. To this end, we would like apply Smereka's semi-implicit method to accelerate the evolution of the associated Euler-Lagrange equations.

For simplicity, as in [Sme03], let's denote the Euler-Lagrange equations as follows:

$$\psi_t = S(\psi), \tag{4.22}$$

then, we can rewrite it as:

$$\psi_t = -\lambda \Delta^2 \psi + \lambda \Delta^2 \psi + S(\psi), \tag{4.23}$$

where Δ^2 is a bi-Laplacian (since (4.14) are fourth order equations) and λ is a parameter. Then we may discretize the equation (4.23) in time as:

$$\psi^{n+1} - \psi^n = dt(-\lambda \Delta^2 \psi^{n+1} + \lambda \Delta^2 \psi^n + S(\psi^n)),$$

and then

$$\psi^{n+1} = \psi^n + dt(1 + dt\lambda \Delta^2)^{-1} S(\psi^n). \tag{4.25}$$

The operator $(1 + dt\lambda \Delta^2)^{-1}$ is a positive definite, and it can be efficiently solved by FFT (Fast Fourier Transformation).

Therefore, in our case, we only need to calculate the values on the right side of (4.14) at time nh as $S(\psi^n)$ for each function ψ_i, then we may get the values of ψ_i at the new time $(n+1)h$ by using FFT.

Smereka's semi-implicit method will relax the CFL condition considerably, since the operator Δ^2 helps to smooth possible high oscillating waves. Numerical experiments in the following section also show that we may choose a much larger time step size than what is required by CFL condition.

4.4.3 Procedure of minimizing NMS functional

During the evolution of ψ_i's by solving (4.14), the intensity unknowns c_i's will also be updated accordingly. By setting $\frac{\partial E}{\partial c_i} = 0$, one may easily get the formulas for updating these intensity variables as follows:

$$c_i = \frac{\int_\Omega f H(\psi_i) \prod_{j=1}^{i-1}(1 - H(\psi_j))}{\int_\Omega H(\psi_i) \prod_{j=1}^{i-1}(1 - H(\psi_j))}, \quad i = 1, ..., n. \tag{4.26}$$

and

$$c_{n+1} = \frac{\int_\Omega f \prod_{j=1}^{n}(1 - H(\psi_j))}{\int_\Omega \prod_{j=1}^{n}(1 - H(\psi_j))}. \tag{4.27}$$

Then, given the initial guesses for the level set functions ψ_i's and the intensity constants c_i's, we iteratively solve the equations (4.14) and (4.26), (4.27).

Now, let's discuss how to choose the initial guesses. We first employ any multi-phase segmentation method, for instance Chan-Vese's method [CV02], to segment the image domain Ω into several regions in each of which the intensity is homogenous, and thus obtain the associated level set function and intensity constant for each region. Then, as in [EM03], we use these results as the initial guesses for solving (4.14) and (4.26), (4.27).

Moreover, the re-initializations of ψ_i's are necessary during the above evolutions. Otherwise, the terms derived from fidelity ones in (4.14) will make ψ_i's keep increasing or decreasing to infinity. On the other hand, the process of re-

initializations can not be taken more frequently since it will prevent the zero level sets from growing.

4.5 Numerical Experiments

In this section, we present some numerical experiments on synthetic images.

4.5.1 Two regions and a background

We here show two examples: Bar and Fork, Ellipse and Disk. For each example, the intensities for the two regions and the background are 1.0, 0.5, and 0 respectively.

The first example is an image with a bar and a broken fork inside a background (Figure 4.2). For this case, there are only two possible orderings: the bar is in front of the fork, or vice versa. For each assumption of ordering, we calculate the Nitzberg-Mumford-Shiota functional. The values are listed as follow:

- Bar front, Fork behind, the NMS functional = 0.1762.

- Fork front, Bar behind, the NMS functional = 0.2718.

This shows that the assumption that the bar is in front of the fork yields a smaller value of the NMS functional, i.e., the scene is made up of a behind fork occluded by a front bar.

In Figure 4.3, we list the evolution process of the two regions under the first assumption of ordering. From these groups of figures, one can see how the broken fork is connecting while the bar is keeping stable especially its corners. It is the
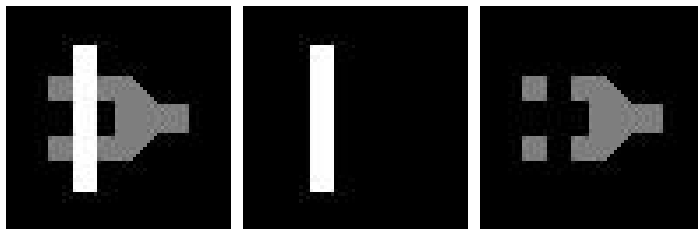
Figure 4.2: Bar and Fork. From left to right, these figures are the original image and the two regions obtained from standard segmentation model.

choice of $\phi(x) = |x|$ when $|x|$ big in (4.2) that preserves the corners. The choice of $\phi(x) = x^2$ will be inevitable to smear these corners.

We omit the evolution process under the second assumption since the two regions are keeping stable.

Moreover, in the experiments, due to the use of Smereka's Semi-Implicit method, we choose the time step size $dt = 5 \times 10^{-4}$, which is far larger than $dt = 10^{-5}$ which is required by the strict CFL condition.

The second example is an image with an ellipse and a crescent inside a background (Figure 4.4). We calculate the values of the Nitzberg-Mumford-Shiota functional for the two ordering as follow:

- Ellipse front, Crescent behind, the NMS functional = 0.1404.

- Crescent front, Ellipse behind, the NMS functional = 0.2812.

This shows that the ellipse is in front of the disk (instead of crescent!). In Figure 4.5, we list the evolution process of the two regions under the first assumption of ordering and we still omit the process under the second assumption. From these

Original image   Two regions by segmentation procedure

Initial   Intermediate   Intermediate   Final
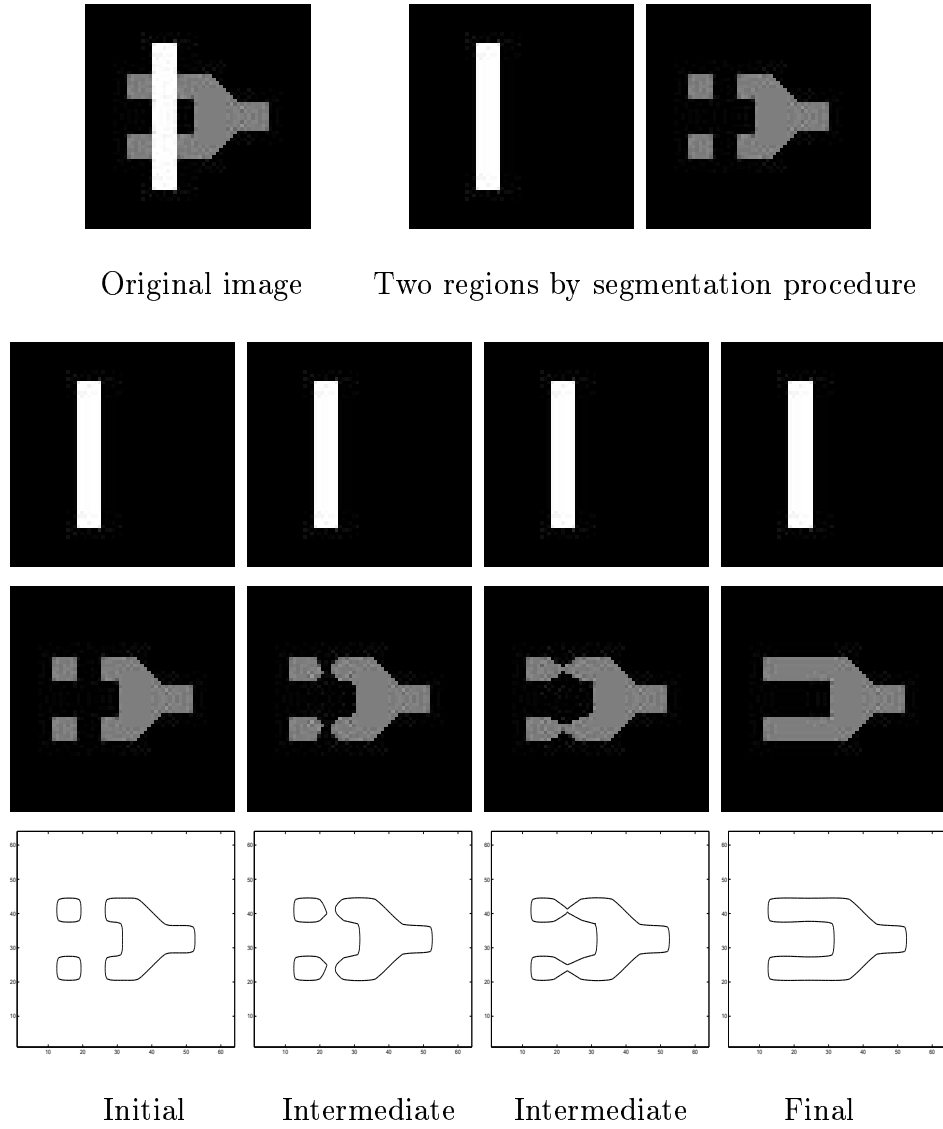
Figure 4.3: The evolution process under the assumption that the Bar is in front of the Fork. In the second and third row, the evolutions of the two regions by solving (4.14) are listed. The fourth row shows how the boundary of the Fork is growing. During the process, the front region occupied by the Bar is keeping stable while the region by the Fork is connecting behind the Bar. In this experiment, the parameters are: $\alpha = 0.00005$, $\beta = 0.005$, and $\lambda = 0.1$ in Smereka's semi-implicit method.
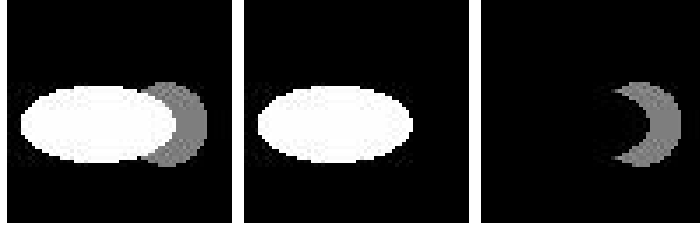
Figure 4.4: Ellipse and Crescent. From left to right, these figures are the original image, and the two regions obtained from standard segmentation model.

groups of figures, one can see how the crescent is growing to be a moon while the front ellipse is keeping stable.

4.5.2 Three regions and a background

We present here an example with an annulus and two bars inside a background (Figure 4.6). The intensities for them are 1.0, 0.9, 0.8, and 0. respectively.

Since there are three objects inside the image, 3! = 6 cases of the ordering should be considered. Here we list the evolution process under the ordering assumption that the Annulus is in front of the vertical Bar while the horizontal Bar is behind the vertical Bar, which yields the smallest value of the Nitzberg-Mumford-Shiota's functional (Figure 4.6).

4.6 Conclusion

In this chapter, we employ level set methods to minimize the Nitzberg-Mumofrd-Shiota functional that appears in the variational formulation of the segmentation with depth problem. Then the minimization of the functional turns out to be solv-

64

Original image   Two regions by segmentation procedure

Initial   Intermediate   Intermediate   Final
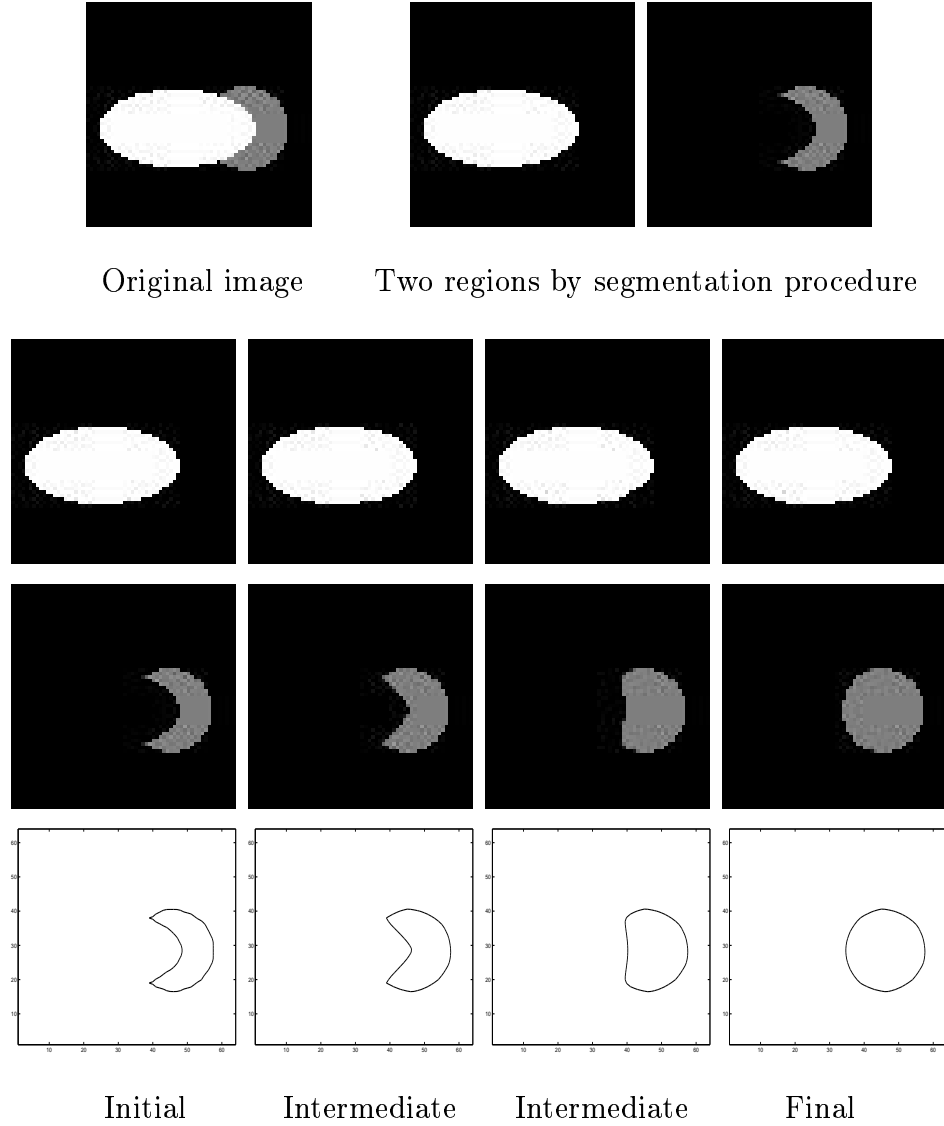
Figure 4.5: The evolution process under the assumption that the Ellipse is in front of the Crescent. In the second and third row, the evolutions of the two regions by solving (4.14) are listed. The fourth row shows how the boundary of the Crescent is growing. During the process, the front region occupied by the Ellipse is keeping stable while the region by the Crescent is connecting behind the Ellipse. In this experiment, the parameters are: $\alpha = 0.00005$, $\beta = 0.01$, and $\lambda = 0.1$ in Smereka's semi-implicit method.
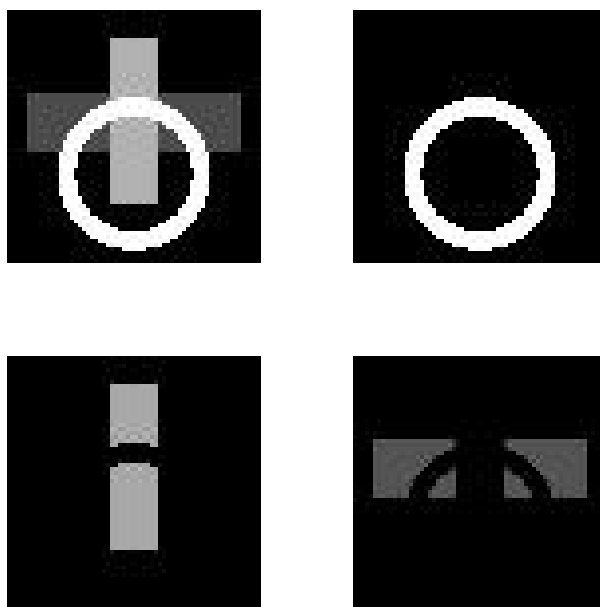
Figure 4.6: An Annulus and two Bars. The top left is the original image, and the other three figures show the regions obtained from the original image by standard segmentation model.

Step 1 (Initial Step)   Step 2 (Intermediate Step)

Step 3 (Intermediate Step)   Step 4 (Final Step)
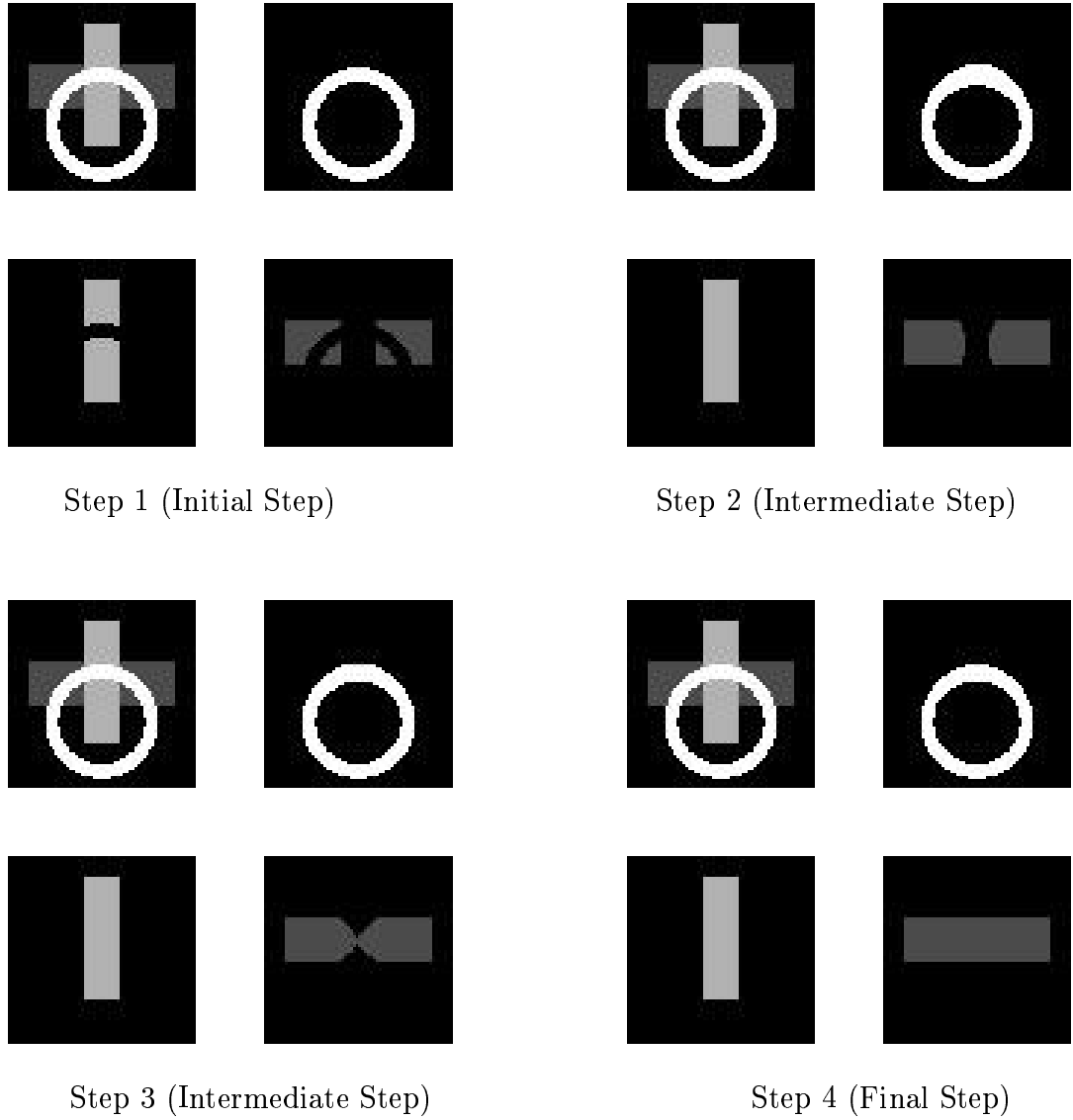
Figure 4.7: The evolution process under the ordering assumption that the Annulus, the vertical Bar, and the horizontal Bar are listed from the nearest to the farthest. In each group of figures, the left top is the original image while the others show the evolution of each regions. During this process, the Annulus is almost keeping stable while the vertical Bar is connecting then the horizontal Bar. In this experiment, we choose the parameters are: $\alpha = 0.00005$, $\beta = 0.03$, and $\lambda = 0.1$ in Smereka's semi-implicit method.

ing a system of fourth order equations. We use Smereka's semi-implicit method to accelerate the evolution of the system. We present some experiments including the cases with two and three objects inside images.

CHAPTER 5

Level set based shape prior segmentation

5.1   Introduction

Segmentation is a fundamental topic in image processing. It is, in brief, a process that segments a given image domain into several parts in each of which the gray intensity is homogeneous.

Numerous approaches have been proposed for this problem. A fundamental PDE-based one is the Mumford-Shah's functional which was discussed comprehensively in [MS95, MS89]. In this approach, the segmentation problem is to find a piecewise smooth function which approximates the image and also prohibits the excessive length of the boundaries between any two contiguous regions. The methodology has brought forth lots of models on segmentation. A direct one is its modified model that approximates the Mumford-Shah's functional via $\Gamma-$ convergence since it is difficult to handle the length of the boundaries. Later, in [CV01, CV02], Chan and Vese proposed a novel, easily handled model that combines the Mumford-Shah's functional and level set methods [OS88], which can handle curves, surfaces with topological changes easily, to the segmentation problem. Besides these models, in [KWT87], Kass et. al. proposed the classic snake model for segmentation and Caselles, et al. developed in [CKS97] a similar

geodesic active contour model.

However, the above models are all intensity based. They fail to segment meaningful objects from images when the objects are occluded by other ones or some parts of them are in low gray contrasts even missing. In fact, these situations always happen in practical applications. Therefore, in these cases, *prior* shape information is needed to successfully segment the desirable objects. The process of segmentation with the incorporation of shape information can be called shape prior segmentation.

There are also many works on shape prior segmentation in the literature. Almost all these work are linear combinations of two terms with one term about some specific segmentation functional and the other about shape difference. For example, in [LGF00], Leventon et. al. presented a model which incorporates statistical based shape information into Caselles' geometric active contours model [CKS97]. Later, Chen et. al. [CTT02] combined a different shape difference term with the same segmentation model. Moreover, in [CTW02], Cremers et al. proposed a shape prior segmentation model which puts a statistical based shape prior into the Mumford-Shah's functional.

In a recent paper, Cremers et al. [CSS03] constructed a variational approach that incorporates a level set based shape difference term [PRR02, RP02] into Chan-Vese's segmentation model. Besides the level set function for segmentation, the authors introduce a new function called labelling function to indicate the regions in which shape priors should be enforced.

In this chapter, based on Chan-Vese's model, we would like to propose a variational model for shape prior segmentation. In this model, we borrow the

idea of Cremer's work in [CSS03], i.e., we also introduce a labelling function. However, Our model is different from Cremer's model in several aspects. Firstly, our approach permits scaling, translation and rotation of prior shapes. Secondly, we take a different shape comparison term which is intrinsic to the objects and the prior shapes, in other words, it is independent of the domain of the image. Moreover, we introduce additional terms to control the labelling function.

The rest of this chapter is organized as follows. In section 5.2, a shape representation via the related signed distance function is discussed. In fact, this review can be found in Chapter 2. However, we still keep it here to make this chapter be complete. In section 5.3, we review some variational models on shape prior segmentation. Then, we detail our variational model in section 5.4. Section 5.5 contains the numerical algorithms, and the experimental results are presented in Section 5.6, which is followed by a conclusion in section 5.7.

5.2   Shape representation via a signed distance function

In [PRR02, RP02], Paragios et. al. represented a shape by the related signed distance function – a special level set function [OS88]. Given an object $\Omega \subset R^2$, which is assumed to be closed and bounded, then there is a unique viscosity solution to the following equation:

$$| \nabla \phi | = 1$$
$$\phi \begin{cases} > 0 \ x \in \Omega \backslash \partial \Omega \\ = 0 \ x \in \partial \Omega \\ < 0 \ x \in R^2 \backslash \Omega. \end{cases} \tag{5.1}$$

Hence, any object in the plane corresponds a unique signed distance function, and vice versa.

As a shape is invariant to translation, rotation and scaling, we may define an equivalent relation in the collection of objects in the plane. Any two objects are said to be *equivalent* if they have the same shape. Their signed distance functions are related. For example, let Ω_1 and Ω_2 be two objects with the same shape, and ϕ_1 and ϕ_2 be the signed distance functions respectively, then there exists a four-tuple (a, b, r, θ) such that:

$$\phi_2(x, y) = r\phi_1[\frac{(x - a)\cos\theta + (y - b)\sin\theta}{r}, \frac{-(x - a)\sin\theta + (y - b)\cos\theta}{r}],$$

$$(5.2)$$

where (a, b) represents the center, r the scaling factor and θ the angle of rotation. In this way, given any object, consequently a signed distance function, we may get the representation of other objects in the equivalence class by choosing the four-tuple (a, b, r, θ).

5.3 A review for shape prior segmentation models

In this section, we review some variational frameworks that are related to our work.

5.3.1 Using prior shapes in geometric active contours (Chen et al.)

In [CKS97], by extending the traditional energy-based active contours (snakes) [KWT87], Caselles et. al. developed over a curve C an energy function $E(C)$,

which reads:

$$\begin{array}{c} min \\ C(q) \end{array} \int g(|\nabla I(C(q))|)|C'(q)|dq, \qquad (5.3)$$

where $I : \Omega \to R$ be an image defined on Ω, and g is a function of the image gradient, which usually takes the form:

$$g(|\nabla I|) = \frac{1}{1 + |\nabla I|^2}. \qquad (5.4)$$

By minimizing the energy $E(C)$, the curve C will be stable on the boundaries of objects in the image, where the gradients of intensity are very large.

In [CTT02], Chen et al. presented a variational framework by incorporating shape priors into Caselles et al.'s model. They proposed a modified procrustes method to describe the shape difference. Let C^* be a curve, called *shape prior* , representing the boundary of an object, and C be another curve, then the difference between curve C and C^*, e.g., the two objects, is defined as:

$$\begin{array}{c} min \\ C(q) \end{array} \int d^2(\mu RC(q) + T)|C'(q)|dq, \qquad (5.5)$$

where μ, R, T be the parameters for scaling, rotation and translation, and $d(x, y) = d(C^*, (x, y))$ is the distance from a point (x, y) to the curve C^*.

Then, by combining these two terms, Chen et al.'s energy for shape prior segmentation reads:

$$E(C, \mu, R, T) = \int \{g(|\nabla I(C(q))|) + \frac{\lambda}{2}d^2(\mu RC(q) + T)\}|C'(q)|dq, \quad (5.6)$$

where $\lambda > 0$ is a parameter. Moreover, they choose $g(|\nabla I|)$ as:

$$g(|\nabla I|) = \frac{1}{1 + \beta|\nabla G_\sigma * I|}, \qquad (5.7)$$

where $\beta > 0$ is a parameter, and $G_\sigma(x) = \frac{1}{\sigma}e^{-|x|^2/4\sigma^2}$.

This model can segment objects, whose shapes are similar to the prior ones, from images even when their complete boundaries are either missing or are low resolution and low contrast.

5.3.2   Segmentation using shape priors and dynamic labelling (Cremers et al.)

In [CV01], Chan and Vese proposed a variational model on a level set function, say ϕ, whose zero level set segments the image domain into several intensity homogenous regions. The functional reads:

$$E(c_1, c_2, \phi) \quad = \quad \int_\Omega \{(u - c_1)^2 H(\phi) + (u - c_2)^2 (1 - H(\phi)) + \mu|\nabla H(\phi)|\}dxdy,$$

$$(5.8)$$

where $u : \Omega \to R$ is an image defined on Ω, c_1 and c_2 are two scalar variables, $H(x)$ is the Heaviside function as follows:

$$H(x) \quad = \quad \begin{cases} 1, & \text{x} \geq 0 \\ 0, & \text{x} < 0, \end{cases} \qquad (5.9)$$

and $\mu > 0$ is a parameter that describes how large the length of the boundaries is permitted, since the term $\int_\Omega |\nabla H(\phi)|$ just represents the length of zero level set of ϕ (see [OF01]).

Recently, Cremers et al. [CSS03] developed a variational approach that incorporates shape priors into Chan-Vese's model. Besides the level set function ϕ, they introduced another function, called the *labelling* function, which will indicate the region where the shape prior should be enforced.

They also adopted Paragios et al.'s method [PRR02] to represent a shape, that is, by means of a signed distance function (Reviewed in section 5.2). Let ϕ be the level set function for segmentation, and ϕ_0 be the one embedding a given shape. Both are signed distance functions. Then the shape difference reads:

$$E_{shape}(\phi) = \int_\Omega (\phi - \phi_0)^2 dxdy. \tag{5.10}$$

Clearly, this integral means that the shape prior is enforced on all the domain Ω, which will affect the segmentation of other objects and fail to segment the desirable object. Consequently, Cremers et al. introduced another function L, called *labelling* function, into the integral. The new shape term takes the form as:

$$E_{shape}(\phi, L) = \int_\Omega (\phi - \phi_0)^2 (L+1)^2 dxdy, \tag{5.11}$$

where L defines the parts of the image domain Ω where the shape prior should be active. For example, the region where $L = -1$ will be excluded from the integral.

As for controlling the area of the region on which the shape prior is enforced and the regularity of the boundary separating the regions, an integral shape prior was developed by Cremers et al. as:

$$E_{shape}(\phi, L) = \int_\Omega \{(\phi - \phi_0)^2 (L+1)^2 + \lambda^2 (L-1)^2 + \gamma |\nabla H(L)|\} dxdy. \tag{5.12}$$

In summary, Cremers et al.'s model is:

$$E(u_+, u_-, \phi, L) = E_{CV}(u_+, u_-, \phi) + \alpha E_{shape}(\phi, L), \tag{5.13}$$

where $\alpha > 0$ is a parameter.

In this paper, Cremers et al. also derived a way to simultaneously optimize the above energy with respect to the level set function ϕ and the labelling function L. For the detail, we refer to [CSS03].

This idea that introducing a labelling function to indicate the region in which the shape prior is enforced is novel. Besides segmenting multiple independent objects in images, the model can also discriminate familiar objects, e.g., whose shapes are similar to the prior shapes, from unfamiliar ones by means of the labelling function. However, the above model does not permit the translation, rotation and scaling of the prior shape or the active contour.

5.4   Our Model

In this section, we detail our model. In section 5.4.1, our model on shape prior segmentation for an image with only one object is explained. Then in section 5.4.2, by introducing a labelling function, we extend the model to general cases that there are probably many objects in the image.

5.4.1   Shape prior segmentation for a simple case

Here, we consider a simple case that there is only one object inside the given image.

Let $u : \Omega \to R$ be the given image defined on the domain Ω, ϕ a level set function for segmentation, and ψ a signed distance function for a given shape. As discussed in section 5.2, let ψ_0 be a fixed signed distance function for the shape, then ψ and ψ_0 are related by a four-tuple (a, b, r, θ) via the formula (5.2).

Instead of taking the shape comparison term as Cremers et al.'s in [CSS03], we define it as follows:

$$E_{shape}(\phi, \psi) \;\; = \;\; \int_\Omega (H(\phi) - H(\psi))^2 dxdy, \tag{5.14}$$

where $H(x)$ is the Heaviside function as stated before. This term is symmetric to ϕ and ψ, and independent of the size of the domain Ω.

Therefore, our model for shape prior segmentation can be written as:

$$E(c_1, c_2, \phi, \psi) \;\; = \;\; E_{CV}(c_1, c_2, \phi) + \lambda E_{shape}(\phi, \psi), \tag{5.15}$$

where $\lambda > 0$ is a parameter.

Due to the relation (5.2) between ψ and ψ_0, we may also write the functional in terms of ψ_0 by replacing ψ with (a, b, r, θ).

We minimize the functional simultaneously with respect to ϕ and ψ (that is, the four-tuple (a, b, r, θ)). The numerical algorithms will be discussed in section 5.5.

5.4.2 Shape prior segmentation for general cases

As stated in section 5.4.1, the shape comparison term (5.14) is defined on all the domain. Hence, it is inapplicable to general cases that there are multiple objects inside the given image, since other objects will contribute to the shape comparison. In this section, our model for general cases is stated.

Besides the segmentation function ϕ and shape function ψ, we also introduce one more level set function L, as called the *labelling* function in Cremers et al's work [CSS03]. Then, the prior shape will be compared with the region where

77

both the level set function ϕ for segmentation and the labelling function L are positive. Consequently, instead of (5.14), the shape comparison term is defined as:

$$E_{shape}(\phi, L, \psi) = \int_\Omega (H(\phi)H(L) - H(\psi))^2 dxdy. \qquad (5.16)$$

Here, $H(\phi)H(L)$ characterizes the intersection of $\{\phi > 0\}$ and $\{L > 0\}$. Ideally, the function L will segment from Ω a region inside which there is only the goal object.

Some restrictions are needed to control the labelling function L. First, if $\{(x, y) \in \Omega : L(x, y) > 0\}$ is empty, the shape comparison term (5.16) will exert no effect on the segmentation process. Therefore, the region in which L takes positive value should be as large as possible. Second, some regularity should be added to the boundary, i.e., the zero level set of L, by which L separates the domain Ω.

Thus, we may rewrite the shape comparison term (5.16) as:

$$E_{shape}(\phi, L, \psi) = \int_\Omega (H(\phi)H(L) - H(\psi))^2 dxdy + \mu_1 \int_\Omega (1 - H(L)) dxdy$$
$$+ \mu_2 \int_\Omega |\nabla H(L)| dxdy, \qquad (5.17)$$

where $\mu_1 > 0$ and $\mu_2 > 0$ are two parameters. In this expression, the second term encourages the area of the region $\{(x, y) \in \Omega : L(x, y) > 0\}$, and the last one smoothes the boundary by which L separates the domain Ω.

However, it is elusive to choose an appropriate μ_1. Too large μ_1 will weaken the action of the labelling function because the region $\{L > 0\}$ will contain other objects besides the desirable object, and on the other hand, if it is so small, L could be stable at a state that the region $\{L > 0\}$ could be smaller than what

78

it should be. Therefore, it is unlikely for the labelling function to control itself independently.

To overcome this difficulty, and notice that when the ideally segmentation for the goal object is obtained, the reference shape function ψ should be also close to segment the object. We therefore introduce an additional term as:

$$E_\psi(\psi, c_1, c_2) \quad = \quad \int_\Omega \{(u - c_1)^2 H(\psi) + (u - c_2)^2 (1 - H(\psi))\} dx dy, \quad (5.18)$$

where c_1 and c_2 are the same variables in Chan-Vese's model (5.8). Generally, this term will be smaller when the region $\psi > 0$ contains larger regions occupied by objects and smaller regions of background. Therefore, the term prevents the reference shape from stopping at a smaller scale than the desirable object. Then, with the interaction between ψ and L in the shape comparison term (5.17), the labelling function L can be controlled less difficultly.

By combining all the above terms (5.8, 5.17, 5.18), our model can be written as:

$$E(\phi, \psi, L, c_1, c_2) \quad = \quad E_{CV} + E_{shape} + E_\psi, \quad (5.19)$$

or explicitly,

$$\begin{aligned} E(\phi, \psi, L, c) \quad = \quad & \int_\Omega (u - c_1)^2 H(\phi) + (u - c_2)^2 (1 - H(\phi)) \\ & + \lambda \int_\Omega (H(\phi) H(L) - H(\psi))^2 \\ & + \mu_1 \int_\Omega (1 - H(L)) + \mu_2 \int_\Omega |\nabla H(L)| \\ & + \nu \int_\Omega (u - c_1)^2 H(\psi) + (u - c_2)^2 (1 - H(\psi)), \quad (5.20) \end{aligned}$$

where $c = (c_1, c_2)$, and λ, μ_1, μ_2 and ν are nonnegative parameters.

Remark 1: In this functional, we omit the length term in E_{CV}. It is partially because that the prior shape may control the smoothness of the zero level set of ϕ to some extend, and on the other hand, without the length term, a fast way for minimizing the functional can be developed, which will be discussed in the following section. However, the length term can be included in the above functional if it is necessary, and then we have to employ the conventional way to decrease the functional.

Remark 2: With the term E_ψ (5.18), the parameters μ_1 and μ_2 become easy to choose. In fact, we fix them for all the experiments listed in this chapter.

5.5 Numerical algorithms

In this section, we discuss the numerical algorithms for minimizing the functionals presented in the last section. We first provide a proof of a fast principle, which is mentioned in [GF02] and similar to Song and Chan's method [SC02], for minimizing Chan-Vese's segmentation model [CV01] without length term. We thus extend the principle to the minimization of our proposed functionals.

5.5.1 Numerical algorithms for the simple case

Recall the functional (5.15):

$$E(c, \phi, \psi) \;\;=\;\; \int_\Omega (u - c_1)^2 H(\phi) + (u - c_2)^2 (1 - H(\phi)) + \lambda \int_\Omega (H(\phi) - H(\psi))^2.$$

Here, we omit the length term in the Chan-Vese's model.

Then, similarly as Chan-Vese's method in [CV01], the minimization of func-

tional (5.15) is performed by solving the following equations (5.21) $\sim$(5.27):

$$c_1 = \frac{\int_\Omega uH(\phi)dxdy}{\int_\Omega H(\phi)dxdy},\tag{5.21}$$

$$c_2 = \frac{\int_\Omega u(1 - H(\phi))dxdy}{\int_\Omega(1 - H(\phi))dxdy},\tag{5.22}$$

and for the shape function ψ, the gradient descents with respect to the four-tuple (a, b, r, θ) are given as follows:

$$\frac{\partial a}{\partial t} = \int_\Omega (H(\psi) - H(\phi))\{\psi_{0x}(x^*, y^*)\cos\theta$$
$$-\psi_{0y}(x^*, y^*)\sin\theta\}\delta(\psi)dxdy,\tag{5.23}$$

$$\frac{\partial b}{\partial t} = \int_\Omega (H(\psi) - H(\phi))\{\psi_{0x}(x^*, y^*)\sin\theta$$
$$+\psi_{0y}(x^*, y^*)\cos\theta\}\delta(\psi)dxdy,\tag{5.24}$$

$$\frac{\partial r}{\partial t} = \int_\Omega (H(\psi) - H(\phi))\{-\psi_0(x^*, y^*) + \psi_{0x}(x^*, y^*)x^*$$
$$+ \psi_{0y}(x^*, y^*)y^*\}\delta(\psi)dxdy,\tag{5.25}$$

$$\frac{\partial \theta}{\partial t} = \int_\Omega (H(\psi) - H(\phi))\{-r\psi_{0x}(x^*, y^*)y^*$$
$$+r\psi_{0y}(x^*, y^*)x^*\}\delta(\psi)dxdy,\tag{5.26}$$

where ψ_0 is a fixed signed distance function representing the given shape, and ψ is related to ψ_0 via (5.2), and

$$x^* = \frac{(x - a)\cos\theta + (y - b)\sin\theta}{r},$$

$$y^* = \frac{-(x - a)\sin\theta + (y - b)\cos\theta}{r},$$

$$\psi_{0x} = \frac{\partial \psi_0}{\partial x}, \qquad \psi_{0y} = \frac{\partial \psi_0}{\partial y},$$

and for the segmentation function ϕ,

$$\frac{\partial \phi}{\partial t} \;=\; -\{(u - c_1)^2 - (u - c_2)^2 + 2\lambda(H(\phi) - H(\psi))\}\delta(\phi), \qquad (5.27)$$

where $\delta(x)$ is the derivative of the Heaviside function $H(x)$ in the distribution sense. In the numerical experiments, as in Chan-Vese [CV01], we choose slightly regularized versions of them as follows:

$$H_\varepsilon(x) \;=\; \frac{1}{2}(1 + \frac{2}{\pi}\arctan(\frac{x}{\varepsilon})) \qquad (5.28)$$

and

$$\delta_\varepsilon(x) \;=\; \frac{1}{\pi}\frac{\varepsilon}{\varepsilon^2 + x^2}, \qquad (5.29)$$

where ϵ is always chosen to be proportional to the mesh size Δx.

In summary, for each iteration in the experiment, we can update c_1, c_2, ψ and ϕ one by one according to formulas (5.21) $\sim$(5.27).

However, due to the fact that we only need the sign of the segmentation function ϕ, we will update it instead of using formula (5.27) but the following principle:

$$\phi \;=\; \begin{cases} 1, & -\{(u - c_1)^2 - (u - c_2)^2 + 2\lambda(H(\phi) - H(\psi))\} \geq 0; \\ -1, & -\{(u - c_1)^2 - (u - c_2)^2 + 2\lambda(H(\phi) - H(\psi))\} < 0. \end{cases} \qquad (5.30)$$

The principle will accelerate the minimization process remarkably. Similar ideas can be found in [GF02, SC02].

In the following, we prove that this kind of principle is equivalent to the conventional method if we consider Chan-Vese's model without length term.

Theorem 2. *Let $u : \Omega \to R$ be a binary image defined on the domain Ω, for simplicity, denoted as $u = \chi_A(x, y)$, where χ_A is the characteristic function of $A \subseteq \Omega$, and $\phi \colon \Omega \times \{t \geq 0\} \to R$ be the segmentation function. Without length term, Chan-Vese's functional reads:*

$$E(c_1, c_2, \phi) \;=\; \int_\Omega \{(u - c_1)^2 H(\phi) + (u - c_2)^2 (1 - H(\phi))\} dx dy,$$

(5.31)

the Euler-Lagrange equation for updating ϕ is:

$$\frac{\partial \phi}{\partial t} \;=\; -[(u - c_1)^2 - (u - c_2)^2] \delta(\phi),$$
(5.32)

and c_1, c_2 are given by (5.21), (5.22). In this case, the principle (5.30) becomes:

$$\phi \;=\; \begin{cases} 1, & -[(u - c_1)^2 - (u - c_2)^2] \geq 0; \\ -1, & -[(u - c_1)^2 - (u - c_2)^2] < 0. \end{cases}$$
(5.33)

Then the minimization of the Chan-Vese's functional by performing (5.21), (5.22) and (5.32) will be equivalent to the procedure by performing (5.21), (5.22) and the principle (5.33).

Proof. For convenience, let us replace c_1, c_2 by $c_1(t)$, $c_2(t)$ in expressions (5.21), (5.22) and (5.32). And without loss of generality, suppose $c_1(0) > c_2(0)$, which are derived from (5.21) and (5.22) with the initial segmentation function $\phi(x, y, 0)$.

We claim that: by performing (5.21), (5.22) and (5.32), the term $(u - c_1(t))^2 - (u - c_2(t))^2$ will keep the sign.

In fact, the amount $(c_1(t) - c_2(t))^2$ will be non-decreasing as $t \to \infty$. This is

83

because:

$$
\begin{aligned}
\frac{dc_1}{dt} &= \frac{(\int_\Omega u\delta(\phi)\phi_t)(\int_\Omega H(\phi)) - (\int_\Omega uH(\phi))(\int_\Omega \delta(\phi)\phi_t)}{(\int_\Omega H(\phi))^2} \\
&= \frac{1}{\int_\Omega H(\phi)}[\int_\Omega u\delta(\phi)\phi_t - c_1(t)\int_\Omega \delta(\phi)\phi_t] \\
&= \frac{1}{\int_\Omega H(\phi)}\int_\Omega (u - c_1(t))\delta(\phi)\phi_t \\
&= \frac{1}{\int_\Omega H(\phi)}\int_\Omega (u - c_1(t))\delta(\phi)[-(u - c_1(t))^2 + (u - c_2(t))^2]\delta(\phi),
\end{aligned}
\tag{5.34}
$$

then, if $c_2(t) < c_1(t)$, thus, $0 \le c_2(t) < c_1(t) \le 1$, it is easy to check that:

$$
(u - c_1(t))[-(u - c_1(t))^2 + (u - c_2(t))^2] > 0,
\tag{5.35}
$$

whenever u takes value 1 or 0. Therefore, $dc_1/dt \ge 0$. On the other hand, if $c_2(t) \ge c_1(t)$, we have $dc_1/dt \le 0$. Consequently,

$$
(c_1(t) - c_2(t))\frac{dc_1}{dt} \ge 0,
\tag{5.36}
$$

similarly,

$$
(c_1(t) - c_2(t))\frac{dc_2}{dt} \le 0.
\tag{5.37}
$$

Combining (5.36) and (5.37), we have:

$$
\frac{d(c_1(t) - c_2(t))^2}{dt} \ge 0,
$$

that is, the amount $(c_1(t) - c_2(t))^2$ is non-decreasing.

By the assumption, $c_1(0) > c_2(0)$, we may arrive that: $c_1(t) > c_2(t)$ for any $t > 0$. Consequently, the term $(u - c_1(t))^2 - (u - c_2(t))^2$ will keep the sign as $t \to \infty$.

Recall (5.32):

$$\frac{\partial \phi}{\partial t} = -[(u - c_1)^2 - (u - c_2)^2]\delta(\phi).$$

Since the right side will never change sign, i.e., the sign is the same as the sign of $-[(u - c_1(0))^2 - (u - c_2(0))^2]$. Therefore, if $-[(u - c_1(0))^2 - (u - c_2(0))^2] > 0$ at point $(x, y) \in \Omega$, $\phi(x, y, t)$ will be positive as $t \to \infty$, otherwise $\phi(x, y, t)$ will be negative as $t \to \infty$. This is just the principle (5.33). $\square$

Remark 3: The theorem shows that it is reasonable to use (5.30) to minimize the functional (5.15) to some extend. On the other hand, it will be unavoidable to view some fuzzy boundaries during the evolution if we apply the principle for very noise images. In this case, we prefer to use the conventional way with the length term.

5.5.2 Numerical algorithms for the general case

We now return to discuss the numerical algorithms for the functional (5.20). Similarly as discussed in the previous section, we update c_1, c_2, L, ψ and ϕ for each iteration in the experiments as follows:

$$c_1 = \frac{\int_\Omega u(H(\phi) + \nu H(\psi)) dx dy}{\int_\Omega (H(\phi) + \nu H(\psi)) dx dy}, \tag{5.38}$$

$$c_2 = \frac{\int_\Omega u((1 - H(\phi)) + \nu(1 - H(\psi))) dx dy}{\int_\Omega ((1 - H(\phi)) + \nu(1 - H(\psi))) dx dy}, \tag{5.39}$$

and

$$\frac{dL}{dt} = -\lambda H(\phi)(1 - 2H(\psi))|\nabla L| + \mu_1|\nabla L|$$
$$+ \mu_2|\nabla L|\nabla \cdot (\frac{\nabla L}{|\nabla L|}). \tag{5.40}$$

As for the shape function ψ, we replace the term $(H(\psi)-H(\phi))$ in (5.23)$\sim$(5.26) by the following one:

$$2\lambda(H(\psi) - H(\phi)H(L)) + \nu[(u - c_1)^2 - (u - c_2)^2], \qquad (5.41)$$

and

$$\frac{d\phi}{dt} = -\delta(\phi)\{[(u - c_1)^2 - (u - c_2)^2] + 2\lambda H(L)(H(\phi)H(\psi) - H(L))\}. \qquad (5.42)$$

To speed up the minimization process, instead of (5.42), we update ϕ with the principle similar to (5.30), which reads:

$$\phi = \begin{cases} 1, & -\{[(u - c_1)^2 - (u - c_2)^2] + 2\lambda H(L)(H(\phi)H(\psi) - H(L))\} \geq 0; \\ -1, & -\{[(u - c_1)^2 - (u - c_2)^2] + 2\lambda H(L)(H(\phi)H(\psi) - H(L))\} < 0. \end{cases} \qquad (5.43)$$

Moreover, we use local level set method, which was proposed by Peng et al. [PMO99], to update the labelling function L, e.g., we only calculate L in a tube around its zero level set instead of the whole domain Ω. All these techniques make the minimization process much more faster than the conventional one. Generally, it always takes 500 iterations for the experiments listed in this chapter.

5.6   Experiment results

In this section, we only present experimental results for the general cases (section 5.4.2) since the simple case (section 5.4.1) can be included in the general one. The experiments include synthetic and real images. For the consistence and

convenience for the choices of the parameters, we normalize the images by scaling them linearly from $[0, 255]$ to $[-1.0, 1.0]$.

5.6.1 Synthetic images

We report here two synthetic images: one is a triangle (close to an equilateral triangle) occluded by other objects (Figure 5.1) and the other is an incomplete triangle with missing part (Figure 5.2). The shape prior is the equilateral triangle.

To view the segmentation process clearly, we list three steps (initial, middle and final) for each function: segmentation function ϕ, labelling function L, shape function ψ and the *goal* segmentation which is represented by the boundary of the region $\{\phi > 0\} \bigcap \{L > 0\}$.

These two examples (Figure 5.1 and Figure 5.2) show that our model can combine intensity information and the prior shape to segment an object with a similar shape even though the object is occluded by other ones or some of its parts are missing.

5.6.2 Real images

In this section, we present two images. One is a hand occluded by other objects (Figure 5.3) and the other is the same hand with some missing parts (Figure 5.4). The prior shape is a similar hand.

To get the signed distance function for the prior shape, we first apply Chan-Vese's segmentation model [CV01] to the image with only a hand inside, then we obtain a level set function φ_0 which is positive inside the hand and negative outside the hand. Secondly, we solve a Hamilton-Jacobi equation (Eikonal equation)

as follows:

$$\frac{\partial \varphi}{\partial t} = \text{sign}(\varphi_0)(1 - |\nabla \varphi|), \tag{5.44}$$

with $\varphi(x,0) = \varphi_0$, to get a signed distance function φ. φ is the signed distance function corresponding to the hand, and defines the prior shape.

The examples (Figure 5.3 and Figure 5.4) listed here validate that our model is also capable of real images, that is, it can segment an object which is similar in shape to the prior one from an image even though the object is occluded by other ones or has some missing parts.

5.6.3 Discussion of our model

The difficulties of segmentation using shape priors lie primarily in several aspects.

Firstly, as shape priors are always employed as templates to supervise the segmentation process, which parts of regions should be affected by the templates? especially when there are other objects in images beside the desirable ones. In this chapter, we borrow Cremers et al.'s idea in [CSS03] by introducing a labelling function to indicate with which part of the segmentation region the prior shape should be compared. Let's recall our model (5.20):

$$\begin{aligned}
E(\phi, \psi, L, c) = & \int_{\Omega} (u - c_1)^2 H(\phi) + (u - c_2)^2 (1 - H(\phi)) \\
& + \lambda \int_{\Omega} (H(\phi) H(L) - H(\psi))^2 \\
& + \mu_1 \int_{\Omega} (1 - H(L)) + \mu_2 \int_{\Omega} |\nabla H(L)| \\
& + \nu \int_{\Omega} (u - c_1)^2 H(\psi) + (u - c_2)^2 (1 - H(\psi)).
\end{aligned}$$

In this functional, the first line is Chan-Vese's model without length term; the

next term measures the shape difference between the prior shape and the region encompassed by $\phi = 0$ and $L = 0$, i.e., the prior shape region $\psi > 0$ is compared with the region $\{\phi > 0\} \bigcap \{L > 0\}$, not $\{\phi > 0\}$; the remain terms in the last two lines describe how the labelling function L will evolve. In fact, it is insufficient for the terms $\mu_1 \int_\Omega (1 - H(L))$ and $\mu_2 \int_\Omega |\nabla H(L)|$ to control the evolution of function L. Therefore, we add more terms as on the last line to indirectly control the evolution of the labelling function L via the shape comparison term. In this way, the parameter μ_1, μ_2 are less difficult to handle. In fact, we fix them and vary only the parameters λ, ν in the experiments listed in this chapter.

Secondly, how to choose the initial guess of the prior shape or shape template, i.e., in this chapter, the shape function ψ? As many other methods, we put the initial prior shapes close to the desirable objects. However, this requirement still can not guarantee that the desirable objects can be segmented. For instance, in Figure 5.3 or 5.4, if the initial shape position of the hand is upside down, one can not expect the correct segmentation of the hand in the image, since the segmentation process could be trapped into local minimizers. Therefore, the initial position of the prior shape is crucial for the final results. We will explore this problem in the future.

5.7 Conclusion

We propose a level set based variational approach that incorporates shape priors into Chan-Vese's model to the shape prior segmentation problem. In our model, besides the level set function for segmentation, as in Cremers' work [CSS03], we introduce another level set function together with the former one to mutually

89

indicate the regions with which the prior shape should be compared. Our model can segment an object, whose shape is similar to the given prior shape, from a background where there are several objects. Moreover, we provide a proof for a fast principle, which is also mentioned [GF02] and similar to [SC02], for minimizing Chan-Vese's segmentation model without length term. We extend the principle to the minimization of our prescribed functionals.

Figure 5.1: The first row lists the original image and the prior shape. From the second row to the fourth row, each column respectively represents the initial, middle and final step of the segmentation function ϕ, labelling function L, shape function ψ, and the goal segmentation which is represented by the boundary of the region $\{\phi > 0\} \bigcap \{L > 0\}$. In this experiment, the parameters chosen are: $\lambda = 4.0$, $\mu_1 = 0.2$, $\mu_2 = 0.2$, $\nu = 2.0$. This example demonstrates that the model can segment the object, which is occluded by other ones and similar to the prior shape, out from a background with several objects.

Original Image   Prior Shape

Initial

Middle
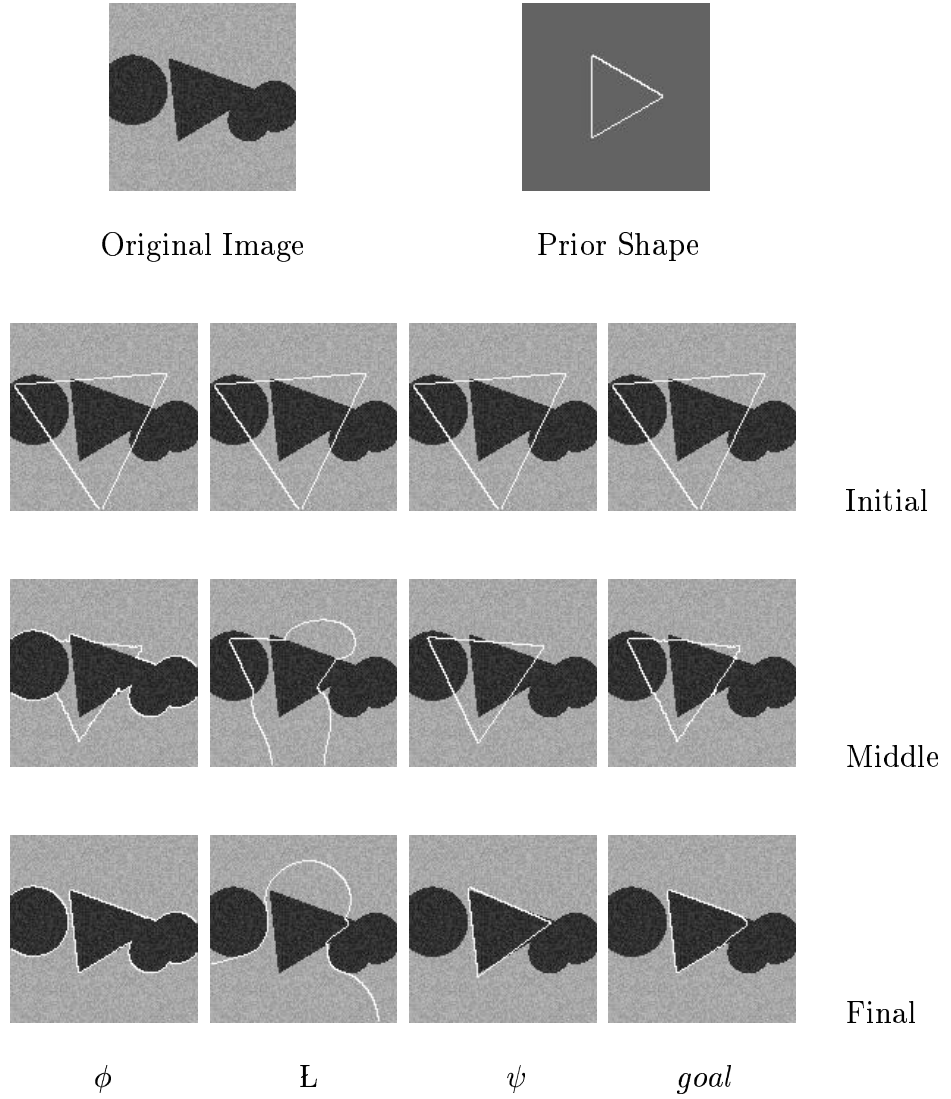
Final

ϕ Ł ψ *goal*

Figure 5.2: The first row lists the original image and the prior shape. From the second row to the fourth row, each column respectively represents the initial, middle and final step of the segmentation function ϕ, labelling function L, shape function ψ, and the goal segmentation which is represented by the boundary of the region $\{\phi > 0\} \bigcap \{L > 0\}$. In this experiment, the parameters chosen are: $\lambda = 6.0$, $\mu_1 = 0.2$, $\mu_2 = 0.2$, $\nu = 0.5$. This example shows that our model is capable of capturing the object similar to the prior shape by filling in it missing parts from an image with several other objects.

Original Image　　　　　　　Prior Shape

Initial

Middle

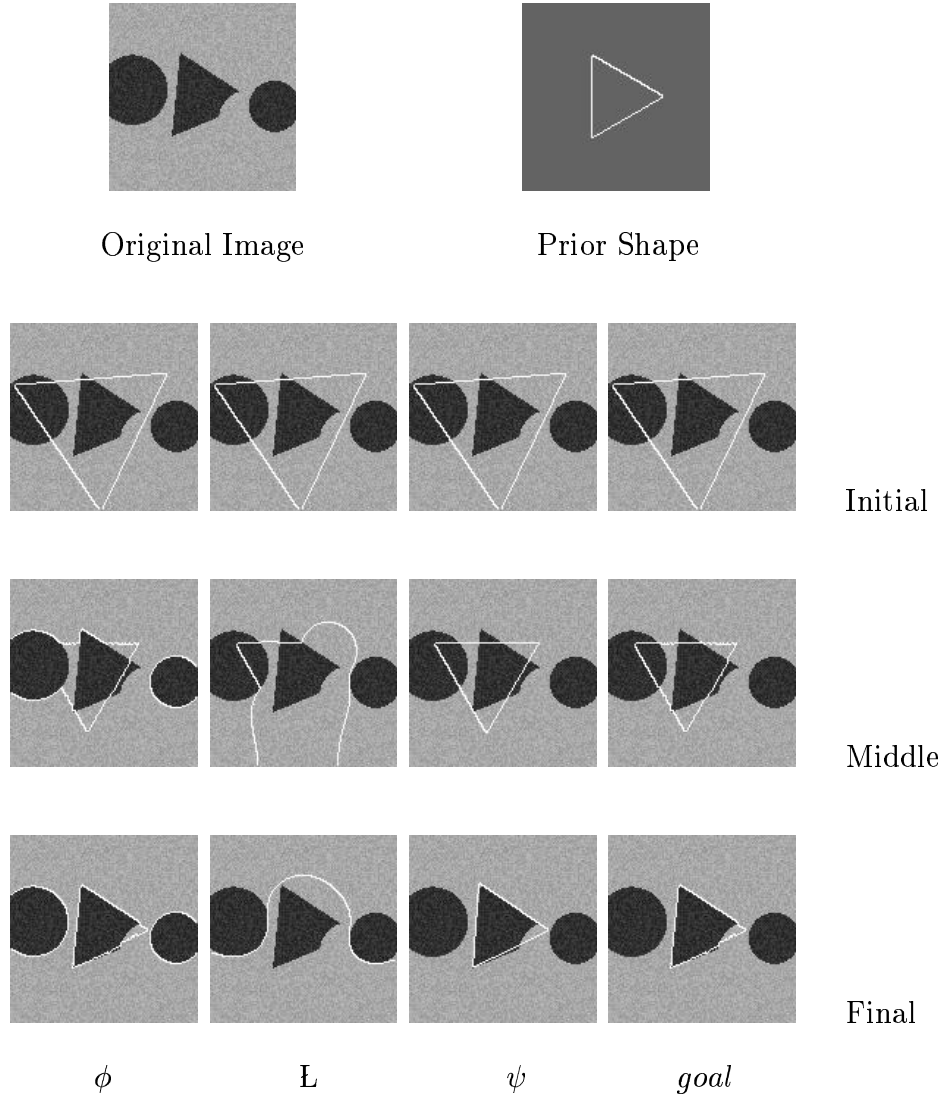Final

ϕ　　　　　Ł　　　　　ψ　　　　*goal*

Figure 5.3: The first row lists the original image and the prior shape. From the second row to the fourth row, each column respectively represents the initial, middle and final step of the segmentation function ϕ, labelling function L, shape function ψ, and the goal segmentation which is represented by the boundary of the region $\{\phi > 0\} \bigcap \{L > 0\}$. In this experiment, the parameters chosen are: $\lambda = 3.0$, $\mu_1 = 0.2$, $\mu_2 = 0.2$, $\nu = 2.0$. This example verifies that our model can capture an object occluded by other ones via the supervision of the prior shape from a real image.

Original Image   Prior Shape

Initial

Middle

Final

ϕ Ł ψ *goal*
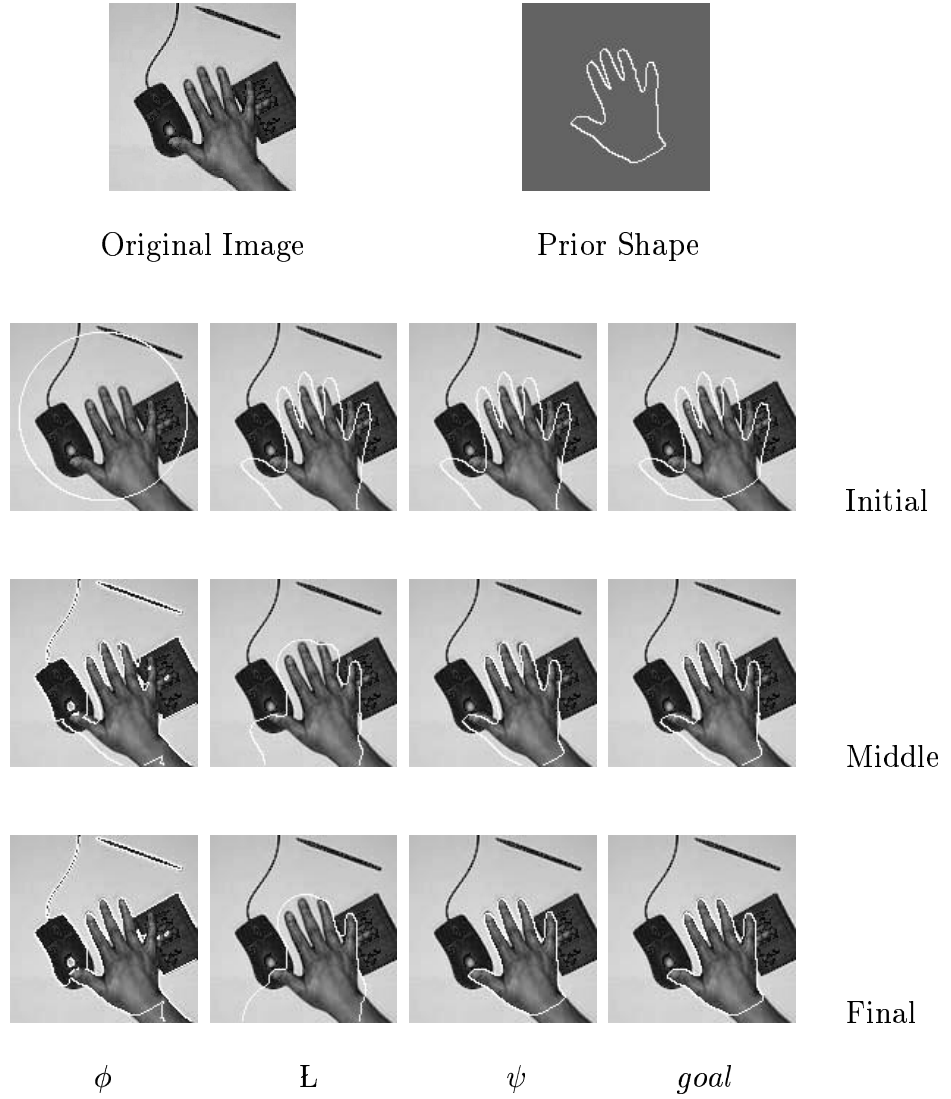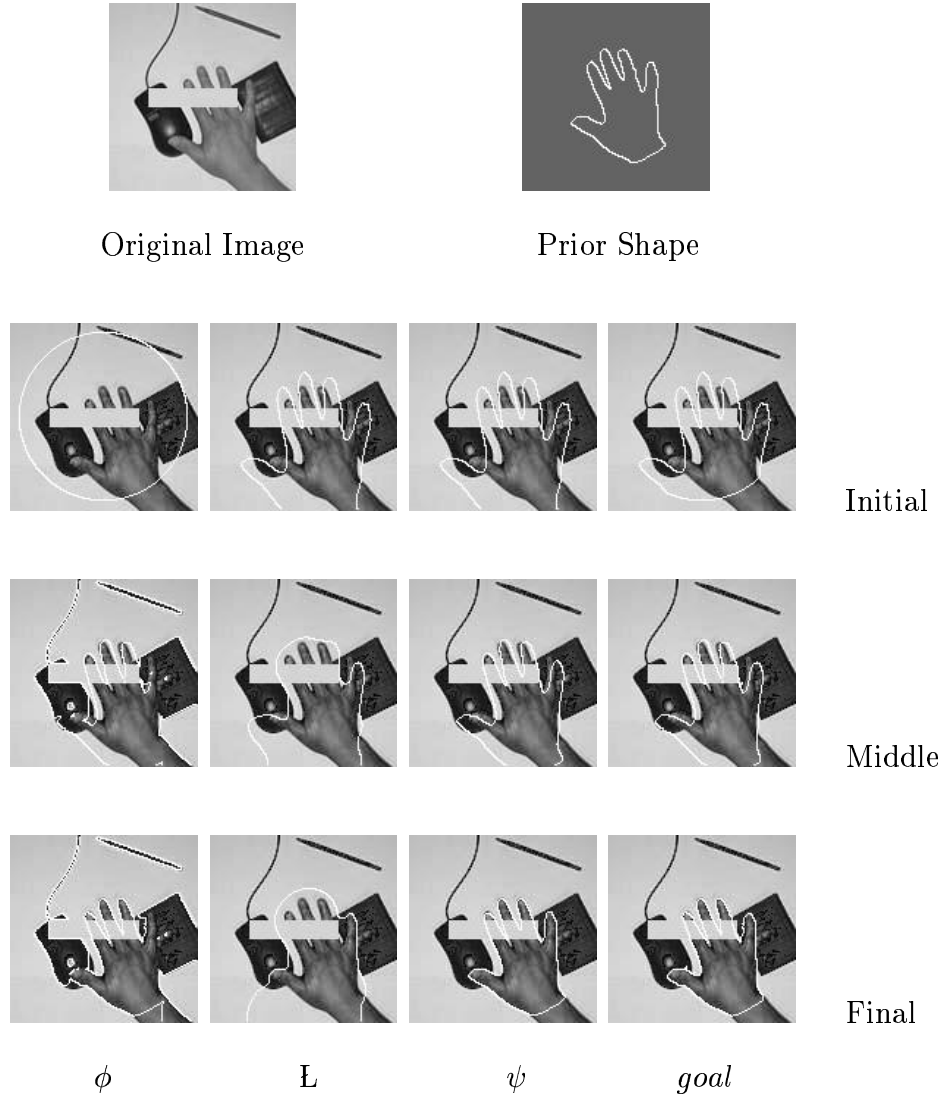
Figure 5.4: The first row lists the original image and the prior shape. From the second row to the fourth row, each column respectively represents the initial, middle and final step of the segmentation function ϕ, labelling function L, shape function ψ, and the goal segmentation which is represented by the boundary of the region $\{\phi > 0\} \bigcap \{L > 0\}$. In this experiment, the parameters chosen are: $\lambda = 2.0$, $\mu_1 = 0.2$, $\mu_2 = 0.2$, $\nu = 2.0$. This example shows that our model can also be applied to segment an object similar to the prior shape by filling in the missing parts from a real image.

REFERENCES

[CKS97]   V. Caselles, R. Kimmel, and G. Sapiro. "Geodesic active contours." *International Journal of Computer Vision*, **22**(1):61–79, 1997.

[CKS02]   T.F. Chan, S.H. Kang, and Jianhong Shen. "Eulers elastica and curvature based inpaitings." *SIAM J. Appl. Math.*, **63**(2):564–592, February 2002.

[CS99]   D.L. Chopp and J.A. Sethian. "Motion by Intrinsic Laplacian of Curvature." *Interfaces and Free Boundaries*, **1**:1–18, 1999.

[CSS03]   D. Cremers, N. Sochen, and C. Schnorr. "Towards recognition-based variational segmentation using shape priors and dynamic labeling." *In L. Griffith, editor, Intl. Conf. on Scale Space Theories in Computer Vision*, **2695 of LNCS**(3):388–400, 2003.

[CTT02]   Y. Chen, H. Tagare, S. Thiruvenkadam, F. Huang, D. Wilson, K. Gopinath, R. Briggs, and E. Geiser. "Using prior shapes in geometric active contours in a variational framework." *International Journal of Computer Vision*, **50**(3):315–328, 2002.

[CTW02]   D. Cremers, F. Tischhauser, J. Weickert, and C. Schnorr. "Diffusion snakes: introducing statistical shape knowledge into the Mumford-Shah functional." *International Journal of Computer Vision*, **50**(3):295–313, 2002.

[CV01]   T.F. Chan and L.A. Vese. "Active contours without edges." *IEEE Trans. on Image Processing*, **10**(2):266–277, February 2001.

[CV02]   T.F. Chan and L.A. Vese. "A multiphase level set framework for image segmentation using the Mumford and Shah model." *International Journal of Computer Vision*, **50**(3):271–293, February 2002.

[EM03]   S. Esedoglu and R. March. "Segmentation with depth but without detecting junctions." *Journal of Mathematical Imaging and Vision*, **18**:7–15, 2003.

[GF02]   F. Gibou and R. Fedkiw. "Fast hybrid k-means level set algorithm for segmentation." *http://math.stanford.edu/ fgibou/*, 2002.

[Gio91]   E. De Giorgi. "Some remarks on Gamma-convergence and least squares methods." *Composite media and homogenization theory*, pp. 135–142, 1991.

[GKP96]   D. Geiger, K. Kumaran, and L. Parida. "Visual Organization for Fig-ure/Ground Separation." *IEEE Conference on Conputer Vision and Pattern Recognition*, June, San Francisco 1996.

[GPR98]   D. Geiger, H.K. Pao, and N. Rubin. "Salient and Multiple illusory surfaces." *IEEE Computer Society Conference on Conputer Vision and Pattern Recognition*, June, San Barbara 1998.

[Kan79]   G. Kanizsa. *Organization in Vision: essays on Gestalt Perception.* Praeger, New York, 1979.

[KWT87]   M. Kass, A. Witkin, and D. Terzopoulos. "Snakes: Active Contour Models." *International Journal of Computer Vision*, **1**(4):321–331, 1987.

[LFG00]   M.E. Leventon, O. Faugeraus, W.L. Grimson, and W.M. Wells III. "Level set based segmentation with intensity and curvature priors." *Mathematical Methods in Biomedical Image Analysis*, 2000.

[LGF00]   M.E. Leventon, W.L. Grimson, and O. Faugeraus. "Statistical shape influence in geodesic active contours." *Proc. IEEE Conf. Computer Vision and Patt. Recog.*,, pp. 316–323, 2000.

[MO00]   A. Marquina and S. Osher. "Explicit algorithms for a new time de-pendent model based on level set motion for nonlinear deblurring and noise removal." *SIAM J. Sci. Comput.*, **22**(2):387–405, 2000.

[MS89]   D. Mumford and J. Shah. "Optimal approximations by piecewise smooth functions and associated variational problems." *Comm. Pure Appl. Math.*, **42**:577–685, 1989.

[MS95]   J.M. Morel and S. Solimini. *Variational methods in image segmenta-tion.* Birkhauser, Boston, 1995.

[Mum94]   D. Mumford. "Elastica and computer vision." *Algebraic Geometry and its applications, C. L. Bajaj, editor*, pp. 491–506, 1994.

[NMS93]   M. Nitzberg, D. Mumford, and T. Shiota. "Filtering, segmentation, and depth." *Lecture Notes in Computer Science*, **662**, 1993.

[OF01]   S. Osher and R. Fedkiw. "Level set methods: an overview and some recent results." *J. Comput. Phys.*, **169**(2):463–502, May 2001.

[OF02]   S. Osher and R. Fedkiw. *Level set methods and dynamic implicit sur-faces.* Springer Verlag, 2002.

[OS88]   S. Osher and J.A. Sethian. "Fronts propagating with curvature-dependent speed algorithm based on Hamilton-Jacobi formulations." *J. Comput. Phys.*, **79**:12–49, 1988.

[PGR99]   H.K. Pao, D. Geiger, and N. Rubin. "Meauring Convexity for Figure/Ground Separation." *In 7th International Conference on Computer Vision*, September Kerkyra, Greece, 1999.

[PM87]   S. Petry and G.E. Meyer. *The Perception of illusory contours.* Springer Verlag, New York, 1987.

[PMO99]   D.P. Peng, B. Merriman, S. Osher, H.K. Zhao, and M. Kang. "A PDE-based fast local level set method." *J. Comput. Phys.*, **155**:410–438, September 1999.

[PRR02]   N. Paragios, M. Rousson, and V. Ramesh. "Matching Distance Functions: A Shape-to-Area Variational Approach for Global-to-Local Registration." *European Conference in Computer Vision*, Copenhangen, Denmark, 2002.

[RP02]   M. Rousson and N. Paragios. "Shape Priors for Level Set Representaions." *European Conference in Computer Vision*, Copenhangen, Denmark, 2002.

[SC01]   A. Sarti and G. Citti. "Subjective surfaces and Riemann mean curvature flow of graphs." *Acta Math. Univ. Comenianae.*, **LXX**(1):85–103, 2001.

[SC02]   B. Song and T. Chan. "A fast algorithm for level set based optimization." *UCLA CAM Report*, 02-68, Decemeber 2002.

[Sme03]   P. Smereka. "Semi-implicit level set methods for curvature and surface diffusion motion." *Journal of Scientific Computing*, **19**(1-3), 2003.

[SMS00]   A. Sarti, R. Malladi, and J.A. Sethian. "Subjective surfaces: A method for completing missing boundaries." *Proceedings of the National Academy of Sciences of the United States of America*, **97**:6258–6263, 2000.

[Ulm76]   S. Ulman. "Filling in the gaps: The shape of subjective contours and a model for their generation." *Biological Cybernetics*, **25**:1–6, 1976.

[ZCM96]   H.K. Zhao, T. Chan, B. Merriman, and S. Osher. "A variational level set approach to multiphase motion." *J. Comput. Phys.*, **127**:179–195, 1996.